Growth and Characterization of Novel Silicon-Based Heterostructures and Device Applications

Cheewee Liu

A DISSERTATION
PRESENTED TO THE FACULTY
OF PRINCETON UNIVERSITY
IN CANDIDACY FOR THE DEGREE
OF DOCTOR OF PHILOSOPHY

RECOMMENDED FOR ACCEPTANCE
BY THE DEPARTMENT OF
ELECTRICAL ENGINEERING

June 1994

© Copyright 1994 by Cheewee Liu.

All rights reserved.

Abstract

We have demonstrated the metastability enhancement of the epitaxial growth on reduced area by selective epitaxial growth of SiGe on patterned Si substrates. A quantitative model of the effect of the selective growth on dislocation density has been developed and compared to experiments. It was concluded that the dominant dislocation nucleation source in the selective areas occurred at the specific heterogeneous sites at the edges of selective areas. This edge nucleation can be controlled by adjusting the orientation of the sidewalls.

We have investigated the reduction of threading dislocation density by graded relaxed buffers and strained layer superlattices. The threading dislocation densities of the completely relaxed films were on the order of $10^7 cm^{-2}$, on which the electron modulation doped structures and the electron resonant tunneling diodes have been successfully fabricated. We also measured the electron effective mass of tensile SiGe on Si for the first time.

We have studied the first chemical vapor deposition growth of strained $Si_{1-x}Ge_x$ alloy layers on $< 110 >$ Si substrates. Compared to the same growth conditions on $< 100 >$ substrates, a slightly lower Ge composition, but a much lower growth rate was observed. From photoluminescence measurements, the bandgap of these films for $0.16 \leq x \leq 0.43$ was determined for the first time, and compared to theory. The conduction band offset was evaluated by the well width dependence of no-phonon luminescence process for the first time.

We have investigated the growth of 3C SiC on Si at the growth temperature from 700 to 1100 °C, using a single precursor (methylsilane) without any carbonization

step. An optimum growth window was found at 800 °C and a "two-step" growth technique was utilized to improve the crystalline quality of the high temperature growth. A positive temperature coefficient of breakdown voltage of Schottky barriers on 3C SiC was observed for the first time. Simple Pt-Schottky barriers fabricated on n-type SiC on Si exhibited a hard breakdown at 60 V.

We have successfully fabricated single crystalline SiGeC random alloys with carbon concentration as high as 1.6 %. The growth with dichlorosilane as a silicon source was more favorable than the silane source in terms of incorporating a large amount of substitutional carbon. The Fourier Transform Infrared Spectroscopy of these alloys exhibited a substitutional carbon at 600 cm^{-1}, with no indication of silicon carbide precipitation.

Acknowledgements

I am indebted to many people for their help and support given to me during my years at Princeton. My advisor, Prof. Jim Sturm, has provided a unique research environment that allowed me to work on the novel Si-based heteroepitaxy. His expertise on growth and devices has given to me an invaluable learning experience and and an endless inspiration. Without his encouragement and advice, none of this work can be successful. I also thank him for giving me the opportunites to present some of this work in several conferences and correcting all the mistakes I made during this work with huge patience.

I would also like to thank Prof. Forrest and Prof. Kahn for reading this work and making helpful comments. They are so kind to read my manuscript in my pressing time constraints.

I am grateful to my colleagues in the Sturm group, Peter Schwartz, Venki Venkataraman, Peter Garone, Xiadong Xiao, Erwin Prinz, Casper Reaves, Zeljka Matutinovic-Krstelj, Qun Mi, Anthony St. Amour, Louis Lanzerotti, Chungchih Wu, Arvind Reddy, and Charles Cullen. I am especially indebted to Anthony St. Amour and Louis Lanzerotti for correcting the English in my manuscript.

Finally, the most important thanks are due to my wife Liehling for her invaluable support, including giving up her own Ph. D. study. I am also indebted to my parents and my son for their love, patience, and support. They should share all the honor from this thesis.

Contents

Abstract iii

Acknowledgements v

1 Introduction 1

1.1 Motivation . 1

Thesis outline 3

2 Strained Layer Epitaxy and Defect Reduction 5

2.1 Introduction . 5

2.2 Lattice structure 6

Electronic structure 11

RTCVD reactor 14

Metastability enhancement by selective growth 17

2.5.1 Model . 17

2.5.2 Experiments and discussion 20

2.5.3 Summary 27

3 Graded Relaxed Buffers for Electron Quantum Devices 28

3.1 Introduction . 28

Growth 32

Characterization 37

Strained layer superlattices 44

Device applications and effective mass measurement 47

4 Growth and Photoluminescence of Strained SiGe on $< 110 >$ Si **50**

4.1 Introduction 50

4.2 Growth 51

Photoluminescence and bandgap 56

Alloy scattering and conduction band offset 61

4.5 Summary 69

5 Structural and Electrical Studies of Low-Temperature β SiC on Si **70**

5.1 Introduction . 70

Growth and characterization 71

Impurity incorporation 79

Schottky barrier fabrication 83

Results and discussion 84

3C SiC HBT emitters 88

Summary 89

6 Single Crystalline SiGeC random alloys **92**

6.1 Introduction 92

Growth and characterization . 93

Summary 96

7 Summary and Future Work **99**

Summary 99

7.2 Future work 100

References **101**

A Processing Notes for Negative Photoresist **115**

B Log-book of Typical Samples Used in This Study **117**

C Growth sequence of sample #1603

D Sample List of SiGeC Alloys

E Publications and Presentations Resulting from This Work

List of Tables

1.1 The recent performance of electronic and optoelectronic devices based on SiGe/Si technology. 2

2.1 The vertical strain and strain energy of coherent $Si_{1-x}Ge_x$ grown on Si substrates with different orientations. 9

3.1 Auger analysis of samples at different annealing conditions. . 37

Summary of effective mass results of tensile strained Si and $Si_{0.94}Ge_{0.06}$ 48

4.1 Summary of the quantum well samples used in the study 52

Summary of SiGeC alloys by DCS growth. 128

Summary of SiGeC alloys by Silane growth. 129

List of Figures

2.1 Coherent growth of the SiGe layer on Si 7

2.2 The thermal equilibrium critical thickness and metastable critical thickness of People and Bean vs Ge fraction 12

2.3 Schematic diagram of the RTCVD reactor 16

2.4 Schematic diagram illustrating concept of selective growth for enhanced metastability. 18

2.5 A schematic plot for enhancement factor vs hole width 19

2.6 The misfit dislocation network of $Si_{0.87}Ge_{0.13}$ layers annealed at 900°C of various periods. 21

2.7 Enhancement factor as a function of square hole width for $Si_{0.87}Ge_{0.13}$. 22

2.8 The number of dislocations in selective area as a linear function of square hole width. 24

2.9 The misfit dislocation network of $Si_{0.8}Ge_{0.2}$ films with different sidewall orientations. 25

2.10 Metastability breakdown of selective areas. 26

3.1 Band edge alignments on various SiGe substrates 30

3.2 Critical thickness and relative residual strain 31

3.3 The idea of graded relaxed buffer 33

3.4 XRD spectra of graded relaxed buffer 36

3.5 XTEM picture of graded relaxed buffers. 38

3.6 plan-view TEM picture of graded relaxed buffer. 41

3.7 plan-view TEM picture of graded relaxed buffer. 42

3.8 EBIC image of the relaxed buffer 43

3.9 XTEM image of SLS's on the relaxed buffer. 45

3.10 High resolution XTEM image of SLS's on the relaxed buffer. 46

3.11 Sample structure for effective mass measurement. 48

3.12 The normalized cyclotron resonance spectra at 4.2K for applied magnetic field as labeled. 49

4.1 Growth rate of SiGe vs germane flow. 53

4.2 Ge content of SiGe vs germane flow. 54

4.3 The Nomarski micrograph of a 0.5μm $Si_{0.71}Ge_{0.29}$ relaxed layer. . . . 55

4.4 PL spectra of strained < 110 > $Si/Si_{1-x}Ge_x/Si$ quantum wells. . . . 58

4.5 The quantum confinement shift measured by 4K PL. 60

4.6 The plot of bandgap vs Ge concentration for both strained (110) and (100) $Si_{1-x}Ge_x$ alloys measured from 77K PL. 62

4.7 NP/TO ratio vs Ge concentration of strained (110) and (100) quantum wells. 63

4.8 Schematic diagram of alloy scattering paths. 64

4.9 The NP/TO ratio vs well width for both (110) and (100) samples . . 67

4.10 ΔE_c as a function of Ge content. 68

5.1 Arrhenius plot of the growth rate of SiC on not-tilted (100) Si. 73

5.2 The XRD spectrum and TEM diffraction pattern of a 750°C-grown film 74

5.3 The XRD spectrum and TEM diffraction pattern of a 800°C-grown film 76

5.4 FTIR spectrum of of a 0.3 μm 800°C grown film. 77

5.5 Raman spectrum of of a 0.3 μm 800°C grown film. 78

5.6 The XRD spectra of a 1000°C film and a "two-step" film. 80

5.7 SIMS plot of SiC multilayers with impurity incorporations. 81

5.8 The chemical concentrations of dopant (P and B) in SiC as a function of the ratios of dopant flow to methylsilane flow. 82

5.9 The I-V characteristics of Al Schottky barriers. 86

5.10 The I-V characteristics of Pt Schottky barriers. 87

5.11 Layer structures of Si BJT and SiC/Si HBT. . 90

The Gummel plots of SiC/Si HBT and Si control device. 91

6.1 The double crystal X-ray rocking curves of SiGeC alloy layers grown by DCS. 95

6.2 FTIR spectra of SiGeC samples grown with DCS at 550 °C. 97

6.3 The double crystal X-ray rocking curves of SiGeC alloy layers grown by silane. 98

Chapter 1

Introduction

1.1 Motivation

The electronic and optical properties of semiconductor heterojunctions have been extensively utilized and studied in the lattice-matched semiconductor materials, such as AlGaAs/GaAs and InGaAsP/InP systems. The lattice match can eliminate the formation of misfit dislocations at interfaces and thus, facilitate the epitaxial growth of device quality materials. More recently, the ability to engineer the dislocations of the mildly lattice-mismatched system, SiGe/Si, opened the gate to fabricate heterojunction devices on Si substrates. This heterojunction technology has the potential advantage of being integrated into the Si-based semiconductor industry, which constitutes 95 % of all semiconductor devices sold worldwide [1]. The promising future of SiGe/Si technology has been further demonstrated by the world's fastest DAC (digital to analog converter) MSI chips, which use SiGe/Si HBT (heterojunction bipolar transistor) technology [2]. With the tremendous strides being made in material engineering of SiGe/Si, the performance of various SiGe devices has been further enhanced. Table 1.1 summarizes the recent figures of merit of various SiGe devices as well as the material technology involved.

For electronic devices, these impressive figures are either compatible or close to those of III-V counterparts and are applicable to practical environments such as

Device	Figure of Merit	Growth Technique
npn-HBT	f_t=113 GHz [3], f_{max}=65 GHz [4]	pseudomorphic
pnp-HBT	f_t=30 GHz [5]	pseudomorphic
n-MODFET	g_m=325 mS/mm at RT, 600 mS/mm at 77K [6]	graded relaxed buffer
p-MODFET	g_m=25 mS/mm [7] at 77K	graded relaxed buffer
n-RTD	P/V=1.2 at RT, 1.5 at 77K [8], 2 at 4K [9]	graded relaxed buffer
p-RTD	P/V=1.6 at 77K, 2.1 at 4K [10]	pseudomorphic
LWIR detector	Schottky barrier:$\lambda_c = 8\mu m$ [11]	pseudomorphic
LED	1.3 μm Q.E.=0.01% [12] at RT	pseudomorphic

Table 1.1: The recent performance of electronic and optoelectronic devices based on SiGe/Si technology. The last column indicates the growth techniques to achieve the device quality material.

the newly opened L band (1-2 GHz) wireless communication. Coupled with the low cost of Si technology, SiGe/Si should play an important role in the high speed market. Furthermore, the tremendous increase of electron and hole mobility ($\mu_n = 180,000 cm^2/Vs$ [13]; $\mu_p = 50,000 cm^2/Vs$ [14]) also provides a promising material system to study semiconductor physics such as fractional quantum hall effect and alloy scattering. However, due to the indirect bandgap of SiGe, the performance of the optoelectronic devices still leaves a lot of room for improvement.

In order to expand the possibilities of Si-based heterostructures, it is desirable to fabricate SiGeC alloys and β-SiC on Si. Due to the wide bandgap (5 eV) and the small lattice constant (50 % smaller than Si) of diamond, the incorporation of substitutional carbon into SiGe may provide a material complementary to SiGe for bandgap engineering and increase the critical thickness of SiGe by compensating the compressive strain of SiGe. Stoichiometric $\beta-$SiC with a band gap of 2.2 eV is a promising wide bandgap material for Si heterojunctions and has been utilized as the emitter of HBTs.

The main purposes of this thesis are to study the growth techniques of SiGe to

achieve high quality material for subsequent device fabrication and to understand the light emission mechanism in SiGe to increase the emission efficiency. Moreover, the growth of SiGeC and β-SiC on Si is studied and utilized for device applications.

1.2 Thesis outline

Nearly all of the advances using SiGe technology to date have involved the blanket growth of strained (pseudomorphic) $Si_{1-x}Ge_x$ alloys on Si (100) substrates. This thesis examines alternative epitaxial growth techniques for expanding the capabilities of column IV heteroepitaxial structures. Chapter 2 reviews the basic concepts of pseudomorphic growth and the growth system (rapid thermal chemical vapor deposition) used in this work. We then demonstrate that the metastability can be enhanced by either low temperature growth or selective growth in oxide holes. The first quantitative model of dislocation filtering by selective growth is proposed. The issue here is to control the misfit dislocations.

In chapter 3, two growth techniques (graded relaxed buffer and strained layer superlattices) to reduce the threading dislocation density are studied. A threading dislocation density in relaxed SiGe on Si as low as $10^6 - 10^7 \mathrm{cm}^{-2}$ has been achieved by using these techniques. High mobility electron gases and electron resonant tunneling diodes have been successfully fabricated on these buffers. Also for the first time, we measure the electron effective mass of tensile-strained SiGe in a modulation doped structure by cyclotron resonance.

Chapter 4 presents the first CVD growth of strained SiGe quantum wells on $< 110 >$ Si substrates. The films exhibit extraordinarily strong no-phonon emission in photoluminescence, compared to that on the $< 100 >$ Si substrates. By varying the well width, the alloy scattering nature of no-phonon emission is confirmed and the dominant process of the alloy scattering is shown to be via an "electron path", rather

than a "hole path". The bandgap of strained $< 110 >$ $Si_{1-x}Ge_x$ vs x has also been experimentally determined for the first time.

In chapter 5, we demonstrate the low temperature growth ($\leq 800°C$) of β SiC on Si by using the methylsilane. The doping incorporations of boron and phosphorus as well as the impurity incorporations of hydrogen and oxygen are investigated. The Schottky barrier fabricated on the n-type β SiC on Si has a record high 60 V hard breakdown voltage. A positive temperature coefficient of hard breakdown voltage is observed for the first time in β SiC.

Chapter 6 presents the growth and material characterization of SiGeC alloys grown at 550°C using methylsilane as the carbon source.

Finally, chapter 7 summarizes the most significant contributions of this thesis and discusses future work which might proceed to further improve the Si-based heterojunction technology.

Chapter 2

Strained Layer Epitaxy and Defect Reduction

2.1 Introduction

Strained layer epitaxy created a wide variety of devices that can not be obtained in lattice-matched systems. The most successful examples are the InGaAs/AlGaAs p-HEMTs (pseudomorphic High Electron Mobility Transistor) which are commercially available as high power microwave transmitters and low noise amplifiers. Semiconductor lasers are another success story in the development of strained layer epitaxy either on GaAs substrates (1.03, 1.07 μm) or on InP substrates (1.3, 1.5 μm). On Si substrates, strained SiGe is making tremendous progress in bipolar transistor technology as well as IR detectors and other novel devices.

The strain in epitaxial layers has two effects, the lattice structure and the electronic structure. The strain in lattice-mismatched systems introduces tetragonal lattice distortion which builds up the elastic energy in the lattice. This limits the maximum thickness (so called critical thickness) of the epitaxial layers without generating defects at the interface. Strain also reduces the bandgap of strained layers relative to relaxed layers, modifies the band structure, and significantly changes the hole effective mass [15, 16] (the effect of strain on the electron effective mass is relatively small, see section 3.5). The lattice aspect and electronic aspect will be discussed in next two sections.

Despite the critical thickness limits, it has been experimentally shown that either low growth temperature or growth on reduced areas [17] can enable metastable pseudomorphic films to be grown over the equilibrium critical thickness limit, which make possible a wider range of applications. In this chapter, we will discuss the reduced area growth technique of SiGe grown on patterned oxide substrates. The main features of our growth reactor will be also described in this chapter.

2.2 Lattice structure

If a $Si_{1-x}Ge_x$ layer with lattice misfit $f = 0.0417x$ is grown fully commensurate on Si as shown in Fig. 2.1, the thin epilayer has to be strained such that SiGe atoms are registered at the same lateral positions as the Si atoms of substrates (The strain in Si substrate is very small due to its relatively large thickness). The in-plane components of the strain are obviously given by

$$e_{xx} = e_{yy} = -f \tag{2.1}$$

A positive sign is used for tension and a negative sign for compression. To find the strain along the growth direction (z), the linear stress-strain equation in the cubic system is used.

$$\begin{pmatrix} \sigma_1 \\ \sigma_2 \\ \sigma_3 \\ \sigma_4 \\ \sigma_5 \\ \sigma_6 \end{pmatrix} = \begin{pmatrix} c_{11} & c_{12} & c_{12} & 0 & 0 & 0 \\ c_{12} & c_{11} & c_{12} & 0 & 0 & 0 \\ c_{12} & c_{12} & c_{11} & 0 & 0 & 0 \\ 0 & 0 & 0 & c_{44} & 0 & 0 \\ 0 & 0 & 0 & 0 & c_{44} & 0 \\ 0 & 0 & 0 & 0 & 0 & c_{44} \end{pmatrix} \begin{pmatrix} e_1 \\ e_2 \\ e_3 \\ e_4 \\ e_5 \\ e_6 \end{pmatrix} \tag{2.2}$$

where σ is the stress tensor; e is the strain tensor; the indices 1, 2, and 3 are the normal components xx, yy and zz, respectively; the indices 4, 5, and 6 are the shear

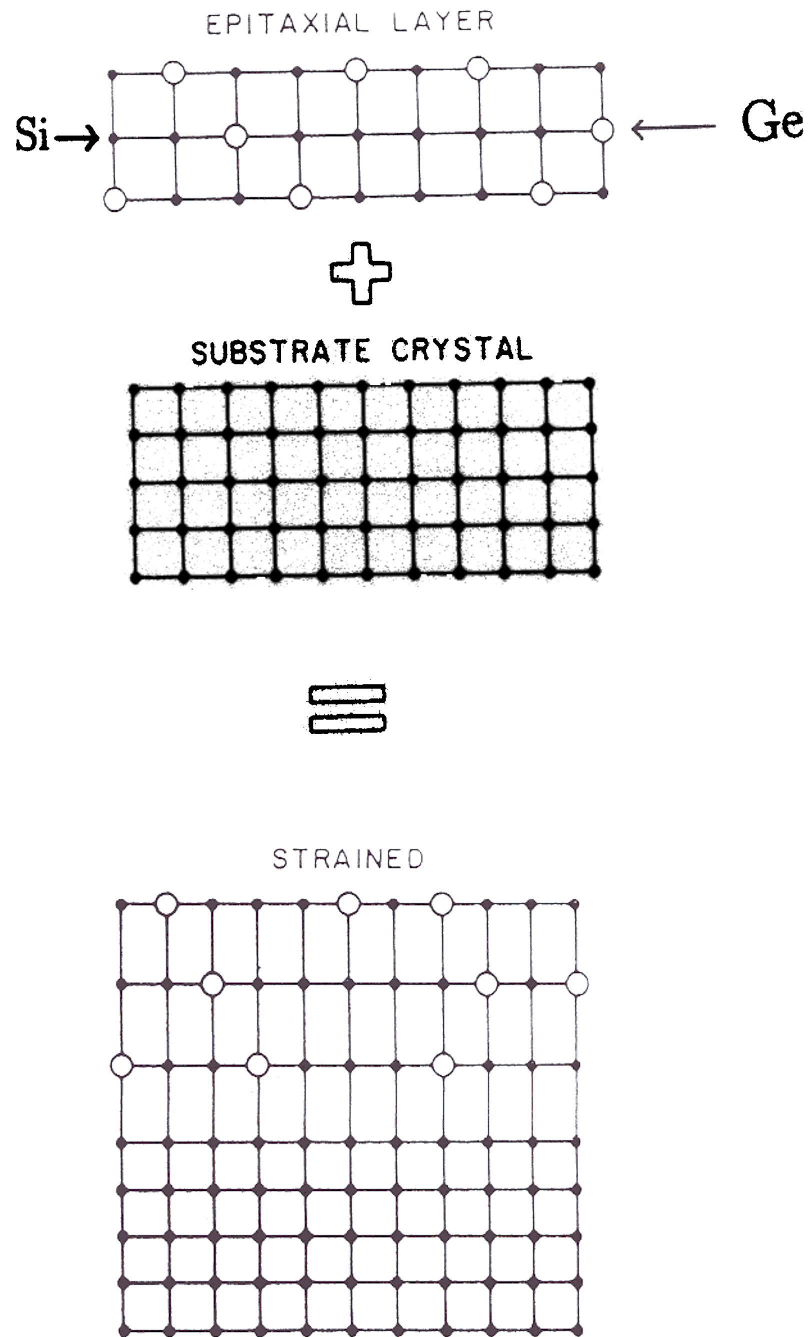

Figure 2.1: Coherent growth of the SiGe layer on Si. The SiGe with a large lattice constant is in-plane compressively strained. (After Ref. [18])

components yz, zx and, xy respectively; and c-tensor elements are elastic constants to determine material properties under strain. Note that if the film is elastically isotropic, then $2c_{44} = c_{11} - c_{22}$. The formal definitions of the strain tensor and the stress tensor can be found in Ref. [19]. With the boundary condition that along the growth direction, the film is free of stress, i.e., σ_3=0 for growth on (001) substrates, the strain along the growth direction is

$$e_{\perp} = e_3 = \frac{2c_{12}}{c_{11}} f \tag{2.3}$$

The energy required to construct such a strained layer is the so called "strain energy". In linear elasticity theory [20], the strain energy density per unit volume for a cubic crystal, E_{ela}, is formulated as

$$E_{ela} = \frac{1}{2}c_{11}(e_1^2 + e_2^2 + e_3^2) + \frac{1}{2}c_{44}(e_4^2 + e_5^2 + e_6^2) + c_{12}(e_1e_2 + e_2e_3 + e_3e_1) \tag{2.4}$$

which can be simplified if the growth is along (100), (110), or (111) orientations [21]. Coordinates, 1, 2, 3, refer to the three 4-fold symmetry axes of cubic crystal, i.e., $< 100 >$, $< 010 >$ and $< 001 >$ directions. The energy density is

$$E_{ela} = f^2 \frac{1}{2}(c_{11} + 2c_{12}) \left[3 - \frac{c_{11} + 2c_{12}}{c_{11} + 2(2c_{44} - c_{11} + c_{12})(l^2m^2 + m^2n^2 + n^2l^2)} \right] \tag{2.5}$$

where l, m and n are the direction cosines of the growth direction. The vertical strain [22] and strain energy per atom are summarized in Table 2.1 for different substrate orientations. Note that the total volume of an atomic unit cell is reduced for all three orientations and the amount of reduced volume is in the order (111) $>$ (110) $>$ (001).

The coherently strained film will not be the most stable configuration, if the thickness of film exceeds some "critical thickness". Besides the strained structure,

orientation	$e_\perp$	value	elastic energy
(001)	$\frac{2c_{12}}{c_{11}}f$	$0.77f$	$39x^2$ meV/atom
(110)	$\frac{c_{11}+3c_{12}-c_{44}}{c_{11}+c_{12}+2c_{44}}f$	$0.51f$	$47x^2$ meV/atom
(110) uniaxial strained	$\frac{c_{11}+c_{12}-c_{44}}{c_{11}+c_{12}+2c_{44}}f$	$0.18f$	$24x^2$ meV/atom
(111)	$2\frac{c_{11}+2c_{12}-2c_{44}}{c_{11}+2c_{12}+4c_{44}}f$	$0.43f$	$49x^2$ meV/atom

Table 2.1: The vertical strain and strain energy of coherent $Si_{1-x}Ge_x$ grown on Si substrates with different orientations under biaxial strain unless noted. The vertical strains on (110) and (111) orientations are calculated in a similar way as (001) strain with different boundary conditions. The elastic constants of Si are used in the numerical value ($c_{11} = 16.48x10^{11}$, $c_{12} = 6.35x10^{11}$ and $c_{44} = 7.90x10^{11}$ dyne/cm^2) [23]. For calculating the strain energy per atom, the Si atomic density $5.0x10^{22}cm^{-3}$ is used.

dislocations also provide another low energy configuration. Since there is no elastic theory to treat dislocations in anisotropic material (like SiGe), the dislocation energy obtained in isotropic elasticity theory [19] is used.

$$E_{dis} = \frac{Gb^2(1-\nu cos^2\theta)}{4\pi(1-\nu)} ln(\alpha h/b) \tag{2.6}$$

where $G = 1/2(c_{11} - c_{12})$ is the shear modulus; $\nu = c_{12}/(c_{11} + c_{12})$ is Poisson's ratio; b is the magnitude of Burger vector; θ is angle between the dislocation line and its Burger vector; α (=4 for most semiconductors) is the core parameter; and the h is the layer thickness.

If the average dislocation spacing is S, the plastic strain is

$$\delta = bcos\lambda/S \tag{2.7}$$

here $bcos\lambda$ is the projection of the Burger's vector on the interface along the normal of dislocation line. The total misfit is

$$f = e + \delta \tag{2.8}$$

where e is the elastic strain. The elastic energy density in eq. 2.5 can be simplified by setting $2c_{44} - c_{11} + c_{12} = 0$ in the isotropic limit.

$$E_{ela} = 2G\frac{1+\nu}{(1-\nu)}e^2 \tag{2.9}$$

The total areal energy of the system is the sum of the elastic energy and dislocation energy.

$$E_{total} = E_{ela}h + E_{dis}/S \tag{2.10}$$

To obtain the thermal equilibrium strain ($e_{thermal}$), the total areal energy is minimized with respect to elastic strain (e). After substituting appropriate values applicable to the SiGe system for parameters $\nu = 0.28$, $cos\theta = cos\lambda = 0.5$, and $b = 4\text{Å}$, we have

$$e_{thermal} = 0.23ln(h)/h \tag{2.11}$$

The critical thickness is defined such that that plastic strain is zero, i.e., $e = f$. By substituting $f = 0.417x$ (x is the Ge content) into eq. 2.11, the well-known "Matthews and Blakeslee" formula in the SiGe system is obtained [24]

$$x = 5.5ln(h_c)/h_c(\text{in Å}) \tag{2.12}$$

However, it has been found experimentally that growth at low temperature (500-700°C) enabled the experimental value of h_c to significantly exceed the thermal equilibrium prediction. The activation barrier of dislocation formation and/or propagation should be responsible for the metastable state formation of SiGe layers. There are a variety of theories to treat the "metastable critical thickness" [25], [26], but no general agreement is concluded. For engineering reference, the simple phenomenological model of People and Bean [25] is often quoted in the literature. The model gives the upper bound of strained layer thickness without dislocation generation.

$$h_c = \frac{0.019\text{ Å}}{\mathrm{f}^2}ln(h_c/4) \tag{2.13}$$

The thermal equilibrium critical thickness and People and Bean's metastable critical thickness are plotted in Fig. 2.2 with the data points from our RTCVD reactor (Rapid Thermal Chemical Vapor Deposition) at a growth temperature of 625 °C. The films with thickness between these two curves can be free of dislocations. Those "metastable" films would like to form dislocations to lower their energy but have not been given enough time at high temperatures to overcome the activation barrier. The RTCVD data were quite consistent with both theories. The metastability of the as-grown strained films in this figure were confirmed by defect etching after annealing at 900 °C for 1 hr.

2.3 Electronic structure

When $Si_{1-x}Ge_x$ layers are coherently grown on (001) Si, the tetragonal distortion will result in biaxial in-plane compression and will lead to tension along the growth direction. Since there are no shear strains, the stain tensor can be written in a simple form.

$$\begin{matrix} f & 0 & 0 \\ 0 & -f & 0 \\ 0 & 0 & \frac{2c_{12}}{c_{11}}f \end{matrix} \quad \frac{2c_{12}+c_{11}}{3c_{11}}f \begin{matrix} 1 & 0 & 0 \\ 0 & -1 & 0 \\ 0 & 0 & 2 \end{matrix} + \frac{2c_{12}-2c_{11}}{3c_{11}}fI \qquad (2.14)$$

where I is the unit matrix. The total strain tensor has been decomposed into a uniaxial component (the first term on the right of the equation, which does not change the volume of the distorted lattice) and a hydrostatic term (the second term on the right of the equation, which does not change the cubic symmetry of the crystal). Due to symmetry considerations, the hydrostatic term will not cause splitting of degeneracies of either the conduction band edges or the valence band edges, and its effect is to shift the relative positions of these edges.

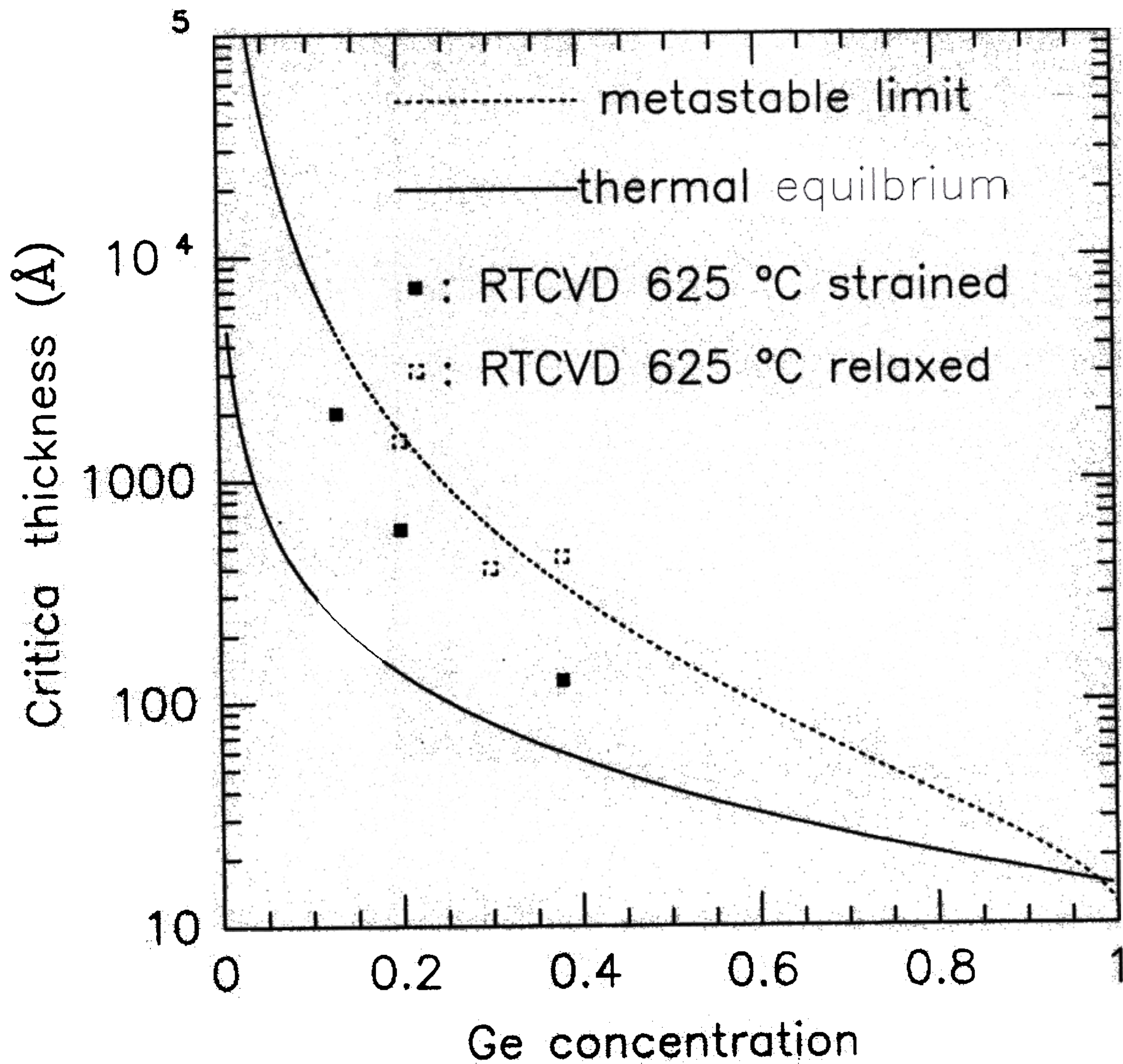

Figure 2.2: The thermal equilibrium critical thickness and metastable critical thickness of People and Bean vs Ge fraction, and the data points for blanket epitaxy in our lab. The films with thickness between these two curves can be free of dislocations. Those "metastable" films would like to form dislocations to lower their energy but have not been given enough time at high temperatures to overcome the activation barrier.

Therefore, the bandgap reduction consists of three terms [27]:

(1) the uniaxial splitting of the degenerate valence band edges (ΔE_1),

(2) the uniaxial splitting of the degenerate conduction band valleys (ΔE_2), and

(3) uniform shifts of the band edges due to the hydrostatic term (ΔE_3).

After solving the 6x6 strain Hamiltonian [28, 27] of the valence band, we have the upshift of the heavy hole band.

$$\Delta E_1 - 2D_u \frac{2c_{12} + c_{11}}{3c_{11}} f \qquad (2.15)$$

where D_u is the valence band deformation potential. This leads to the upshift valence band edge (heavy hole in this case)

After solving the Herring-Vogt equation(Eqn.5 in Ref.[27]), the conduction band edges for the four valleys perpendicular to the growth direction are shifted to lower energy under the compressive strain. The magnitude of the shift is

$$\Delta E_2 - \Xi_u \frac{2c_{12} + c_{11}}{3c_{11}} f \qquad (2.16)$$

where Ξ_u is the uniaxial conduction band deformation potential.

The hydrostatic term also leads to the uniform upshift of the valence band and the uniform downshift of the conduction valleys. It is given as

$$\Delta E_3 \quad (\Xi_d \quad \frac{\Xi_u}{3} \quad a) \frac{c_{12} - 2c_{11}}{c_{11}} f \qquad (2.17)$$

where Ξ_d is the dilation deformation potential for conduction band, and a denotes the valence band deformation potential of hydrostatic strain.

The results of these three terms are combined to obtain the total bandgap reduction due to strain. As a numerical note, ΔE_2 contributes about one half of the total bandgap reduction, the other terms each contribute about one quarter of the total reduction of the bandgap in the region of small Ge content. For example, ΔE_1, ΔE_2,

and ΔE_3 of a $Si_{0.8}Ge_{0.2}$ strained layer are 25, 40, and 26 meV, respectively, using the material parameters in Ref. [27]. By combining the measured bandgap of relaxed $Si_{1-x}Ge_x$ and the self-consistent *ab initio* pseudopotential calculation of strained Ge on Si, the band alignments can be also determined [29].

2.4 RTCVD reactor

In this section, we describe the Rapid Thermal Chemical Vapor Deposition (RTCVD) reactor in our lab which is a combination of rapid thermal processing and chemical vapor deposition [30]. All the samples studied in the thesis were grown in this reactor with different growth parameters (gas sources, flows, pressure, temperature, etc.). A schematic diagram of the reactor is shown in Fig. 2.3. The reactor is a non-UHV chamber consisting of a cylindrical quartz growth tube in which a single 100 mm Si wafer sits on a quartz stand and a diffuser is placed after the gas inlet to reduce the turbulent flows. The outside of the tube is cooled by nitrogen, and the gold plated reflector is cooled by water. After RCA (1 HCl: 1 H_2O_2: 5 H_2O 10 min. / 1 NH_4OH : 1 H_2O_2: 5 H_2O 10 min.) or silicon valley (1 H_2O_2: 2 H_2SO_4 20 min.) cleaning, the wafer is given a dip in 50:1 HF (50 part DI water and 1 part HF, no DI water rinse after HF dip), then transferred into the reactor tube through a load lock which reduces residual oxygen contamination in the epitaxial films to less than 10^{18} cm^{-3}, which is the detection limit of Secondary Ion Mass Spectroscopy (SIMS). This ensures high carrier lifetime in our films [31]. The RCA cleaning is necessary for selective growth on oxide patterned wafers to completely remove the photoresist on the wafer surface. Then, the wafer is heated up to 1000°C for in-situ hydrogen cleaning at a pressurre of 250 torr by a twelve-tungsten-halogen-lamp illuminator which allows for rapid temperature switching and growth temperature optimization for each individual epitaxial layer in a multilayer sample. The temperature is monitored by detecting the

transmission of 1.3μm and 1.5μm infrared light from semiconductor lasers through the wafer [32]. A feedback system controls the wafer temperature accurately to within a few degrees for a growth temperature lower than 800 °C. This is important because the growth rates depend exponentially on temperature in the surface-reaction limited region.

The gases used are dichlorosilane ($SiCl_2H_2$) and silane (SiH_4) for silicon and germane (0.8% GeH_4 in H_2) for germanium. The doping is accomplished simply by introducing phosphine (70 ppm PH_3 in H_2) or diborane (10 ppm B_2H_6 in H_2) into the gas mixture. The gas mixture is established in a hydrogen carrier gas prior to being injected into reactor and is exhausted through a burn box by a mechanical pump. Under a typical growth pressure of 6 torr, silicon layers are grown at 700°C (30 Å/min) and 1000°C (0.2 μm/min) using 26 sccm of dichlorosilane in 3 slpm of hydrogen. The $Si_{1-x}Ge_x$ layers are grown at 625°C by adding germane to this mixture, depending on the Ge content required. The growth conditions for other materials will be described in each chapter, when a new material is grown.

The RTCVD system has generated a variety of high quality material for both device applications and physics studies. These included heterojunction bipolar transistors (HBTs) with near-ideal base currents and high Early voltages [33, 34], strained Si/SiGe/Si quantum wells with the first band-edge photoluminescence [35], long wavelength IR detectors [11], electron resonant tunneling diodes [9], and electron modulation doped structures [36]

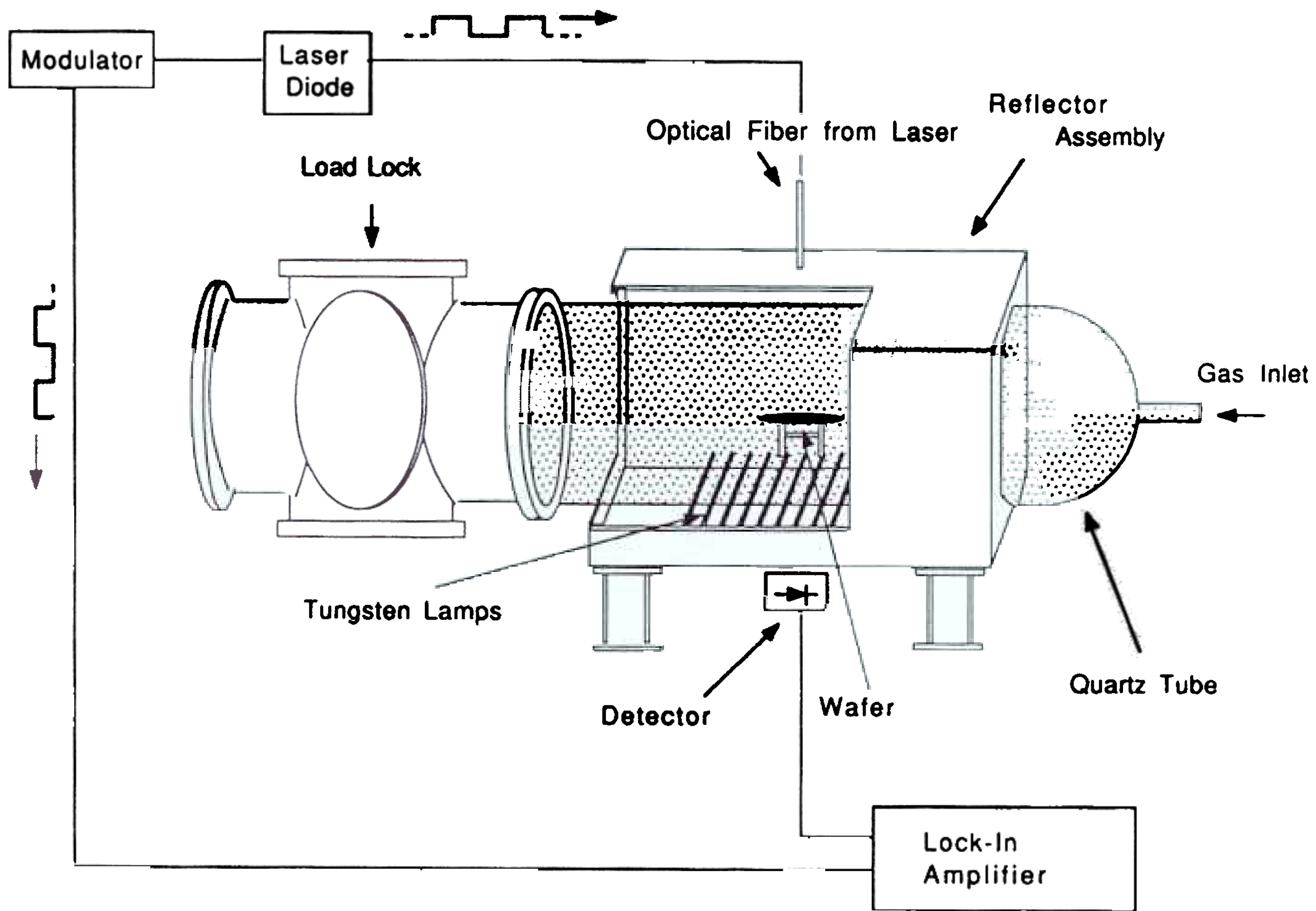

Figure 2.3: Schematic diagram of the RTCVD reactor. Key features are labeled in the figure.

2.5 Metastability enhancement by selective growth

For the extension of the applications of strained layers, the reduction of the dislocation densities of layers with thickness exceeding the equilibrium critical thickness is necessary. This can be achieved by growth on reduced areas. The selective epitaxial growth in oxide holes is studied for this purpose. Previous studies [37, 38] indeed qualitatively demonstrated the metastability of as-grown films by both Chemical Vapor Deposition and Molecular Beam Epitaxy in patterned oxide or on mesas. In this work, the thermal stability after post-growth annealing is investigated and a quantitative model of the metastability enhancement in selective areas is developed.

2.5.1 Model

The relaxation of strained $Si_{1-x}Ge_x$ layers occurs through the nucleation and subsequent propagation of misfit dislocations. Because of the long dislocation length, misfit dislocations can affect areas far from their original nucleation sites. The concept of selective area growth is to reduce the range over which a dislocation can propagate. Fig. 2.4(a) shows the area over which dislocation nucleation will affect the central WxW area of interest, assuming an average dislocation length L. The number of dislocation lines N in the central WxW area is given by

$$N = \alpha(2LW + W^2) \tag{2.18}$$

where W is the width of the square holes and α is the areal density (cm^{-2}) of nucleation sites. If the same WxW area is surrounded by field oxide as in Fig. 2.4(b), the selective area is susceptible only to dislocations nucleated within this WxW area, but possible nucleation from the edge of the selective areas must be taken into account. The number of dislocations in the selective area, N_s is determined by

$$N_s = \alpha W^2 + 4\beta W \tag{2.19}$$

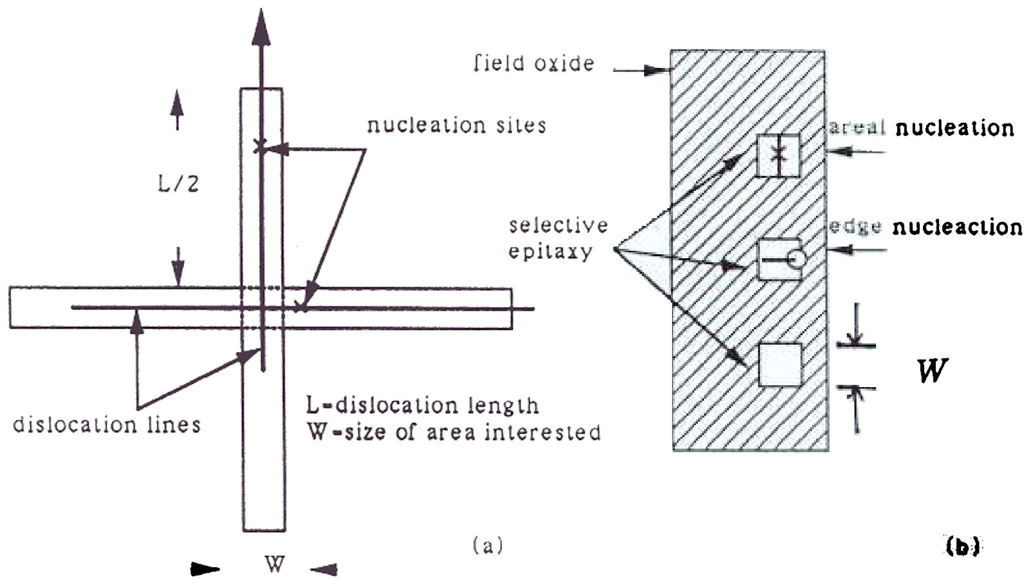

Figure 2.4: Schematic diagram illustrating concept of selective growth for enhanced metastability.

where β is linear density (per cm) of nucleation sites on the edge of oxide. We assumed W is less than the dislocation length, which is true in practice due to high dislocation propagation velocity at the annealing temperature of 900 °C. The ratio of N and N_s, i.e., the ratio of the numbers of dislocations in a given area for blanket vs selective epitaxy, is defined as enhancement factor (EF) of the metastability of the selective structure,

$$EF = \frac{N}{N_s} = \frac{W + 2L}{W + W_0}, \quad W_0 \equiv \frac{4\beta}{\alpha} \tag{2.20}$$

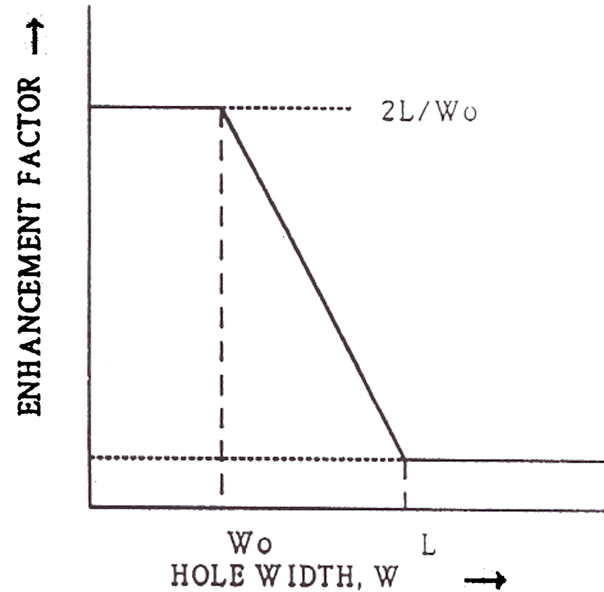

Figure 2.5: A schematic plot for enhancement factor vs hole width. The enhancement factor has a limiting value of unity for large W as one approached the non-selective case. For very small W, the edge nucleation will be dominant, so that the enhancement factor is again independent of W. The EF will be greater or less than unity depending on the relative severity of edge nucleation compared to the dislocation length. For intermediate W, EF varies monotonically between these limiting values and is given by $2L/W$.

The enhancement factor has a limiting value of unity for large W as one approaches the non-selective case. For very small W, $EF = 2L/W_0$, the edge nucleation will be dominant, so that the enhancement factor is again independent of W. The EF will be greater or less than unity depending on the relative severity of edge nucleation compared to the dislocation length. For intermediate W, EF varies monotonically between these limiting values and is given by $2L/W$. The relationship is schematically sketched in Fig. 2.5, assuming $L > W_o$.

2.5.2 Experiments and discussion

To study the effect of growth area on metastability, we grew 2000 Å of epitaxial $Si_{0.87}Ge_{0.13}$ (sample 701) selectively in various size of square holes in thermal oxide on Si (001) wafers at 625°C by RTCVD with square hole edges oriented along $< 110 >$ direction. The 0.5 μm thick oxide pattern was defined by lithography using negative photoresist, and then, etched by buffered oxide etch. Before SiGe deposition, an 80 nm Si buffer was grown selectively at 900 °C, and a selective Si cap of 4 nm was grown on the top of SiGe. No epitaxial layers were observed on the oxide under the Nomarski microscope. After the growth, the samples were annealed at 900°C for different periods. The dislocations were then delineated by defect etching [39], with 4 parts 49% HF and 5 parts 0.3M CrO_3, and observed under a Nomarski microscope. For reference, the thermal equilibrium critical thickness of $Si_{0.87}Ge_{0.13}$ is 230 Å, estimated from Eqn. 2.12.

No dislocations were observed for as-grown $Si_{0.87}Ge_{0.13}$ layers within selective areas, and for the non-selective areas, the spacing between dislocations was on the order of 1 cm. The samples with various annealing times all showed that the selective areas were less defective than the non-selective areas (Fig. 2.6). The independence of the enchancement factor versus hole width for 5 min. annealed samples (Fig. 2.7, average over 20 samples) implies that W is less than W_o, i.e., dislocations in the selective areas are primarily generated by edge nucleation. The low value (~2) of enchancement factor further supports the conjecture, because the enhancement factor should be around 1,000 for L=1cm and W=20 μm if there were no edge nucleation ($W_0 = 0$). The dislocation length L was determined by looking at the dislocation length on the unpatterned areas.

After annealing for 1 hr. and 2 hr., the dislocation lines on non-selective areas were too close to count reliably. But X-ray diffraction showed no visible shift of strained $Si_{0.87}Ge_{0.13}$ peak within the resolution of $\Delta 2\theta = 0.03°$. Because the dif-

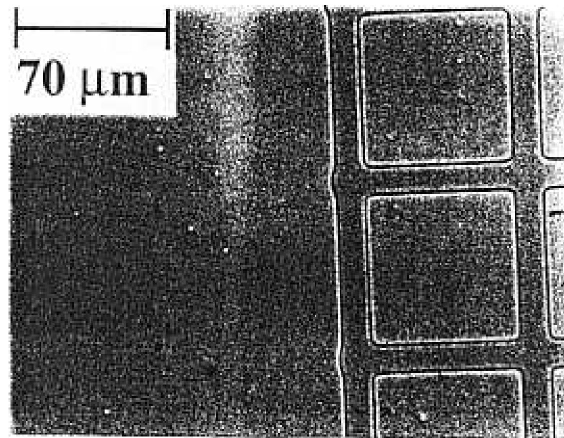

(a) as-grown

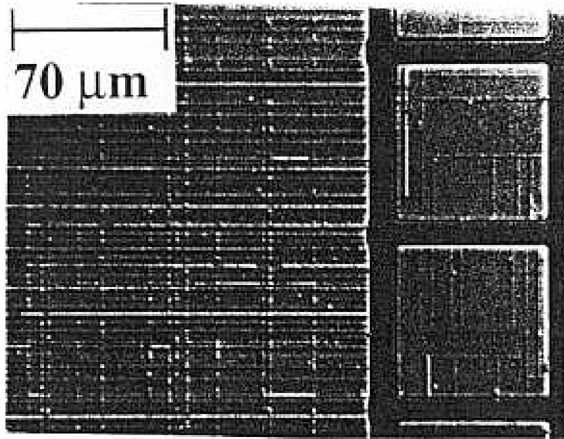

(b) 5 min

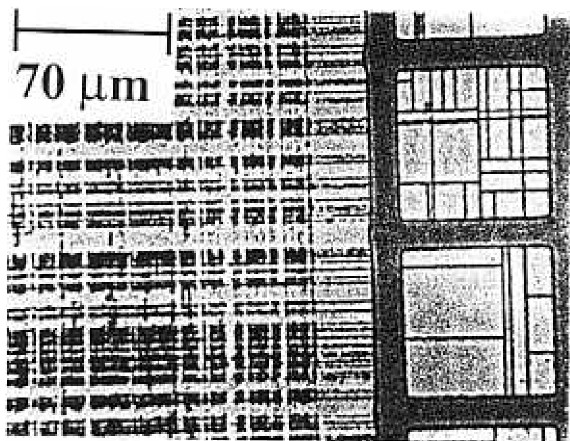

(c) 60 min

Figure 2.6: The misfit dislocation network of $Si_{0.87}Ge_{0.13}$ layers annealed at 900°C in nitrogen of various periods for growth in large areas and in 70 μm holes.

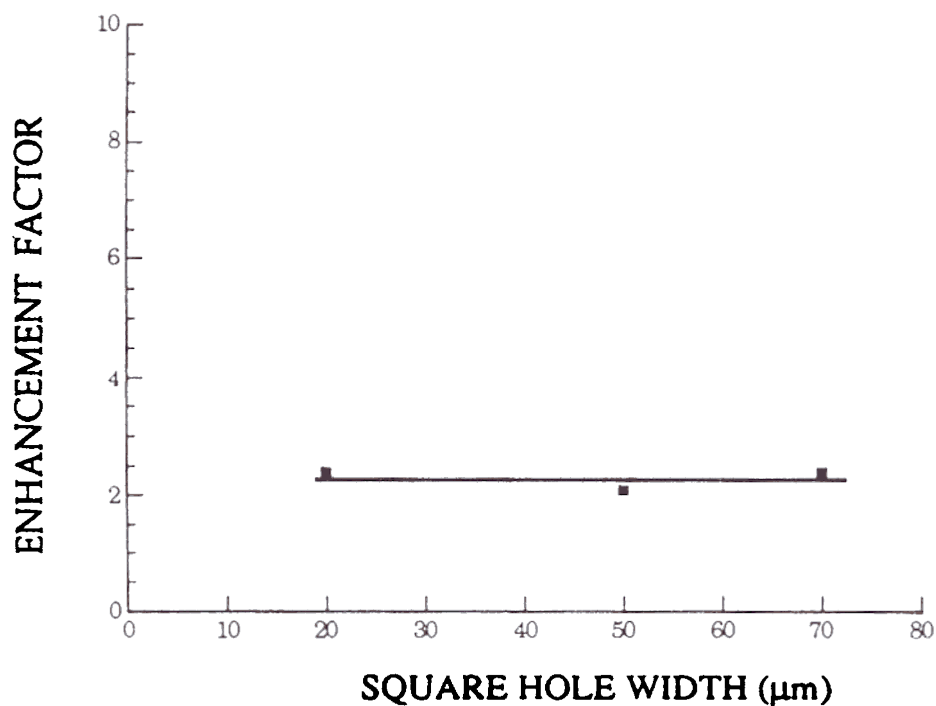

Figure 2.7: Enhancement factor as a function of square hole width for $Si_{0.87}Ge_{0.13}$ after 5 min. annealing at 900°C. The constant enhancement factor indicates W less than W_o, i.e., the edge nucleation is dominant.

ference between the strained (400) CuKα peak and the relaxed (400) CuKα peak of $Si_{0.87}Ge_{0.13}$ was about 0.3°, the relaxation of these films was less than 10 %, indicating an average spacing of dislocation lines more than 0.4 μm (the average spacing of fully relaxed layers is about 40 nm). Combined with a dislocation spacing in the selective area of 8 μm or so, the enhancement factor is estimated to be less than 20, consistent with the previous arguments.

To further confirm the edge nucleation mechanism, we plot the number of dislocations versus hole width in Fig. 2.8 for these three annealing times to compare data to Eqn.2.18. The linear dependence of the number of dislocations versus hole width indicates that the edge nucleation was dominant over the areal nucleation. Further evidence in support of edge nucleation is that the dislocation patterns in selective areas had at least one termination of the dislocations on the oxide. If areal nucleation dominates, there should be some chance that the dislocations would be terminated within selective areas due to their intersection by other dislocations.

In Fig. 2.8, one can see that the number of dislocations hardly increases from 5 min. to 120 min. of annealing. The number of homogeneous nucleation sites should linearly increase with time, because of the similar activation energy in these films in this small relaxation region (within 10 %) [40]. Therefore, we conclude that the edge nucleation sites occurred at some specific heterogeneous sites, possibly associated with structural defects at the interface of the oxide sidewalls and the selective epitaxial layers.

The edge nucleation was also investigated in a set of samples with 150-nm thick selective $Si_{0.8}Ge_{0.2}$ grown in oxide holes aligned in $< 110 >$ direction (sample 498) and with 200-nm thick selective $Si_{0.8}Ge_{0.2}$ grown in oxide holes aligned in $< 100 >$ direction (sample 719). The as grown $< 110 >$-aligned structure had a high defect density in both selective and non-selective areas (Fig. 2.9(a)). In the $< 100 >$ aligned samples, however, the defect density in selective areas was remarkably re-

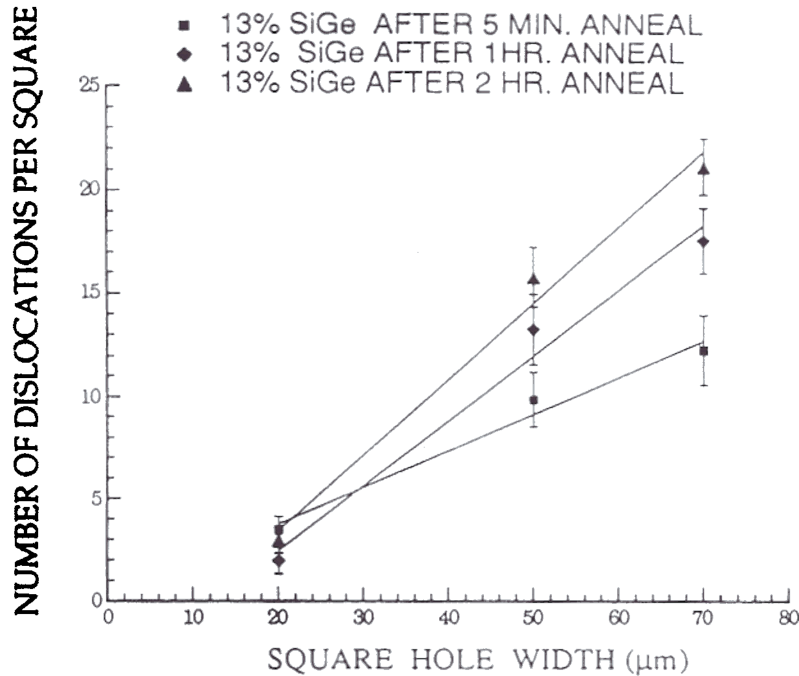

Figure 2.8: The number of dislocations in selective area as a linear function of square hole width for 200 nm $Si_{0.87}Ge_{0.13}$ with various annealing time at 900°C.

duced (Fig. 2.9(b)), despite the greater $Si_{0.8}Ge_{0.2}$ thickness. This implies a lower heterogeneous nucleation site density on $< 100 >$ aligned sidewalls. Lower defect densities are indeed commonly observed in selective homoepitaxial silicon layers with hole edge oriented in the $< 100 >$ direction [41]. This supports the hypothesis that the edge nucleation sites are related to some defects at oxide sidewalls.

However, if the samples were annealed continuously up to 13 hr. at 900°C some of the selective areas exhibited abnormally large numbers of dislocations, while most other selective areas remained to have relatively small numbers of dislocations(Fig. 2.10). The reason for this breakdown of metastability is not clear at this point. However, this effect has also been observed in InGaAs/GaAs material system [40].

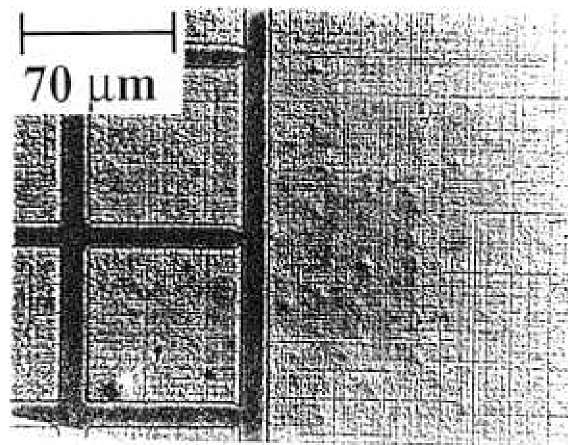

(a) { 10}

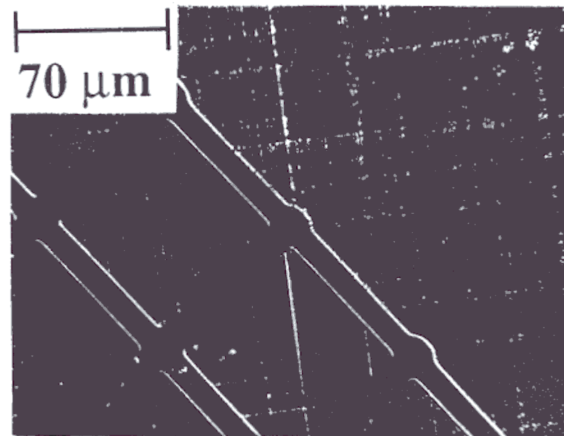

(b) {100}

Figure 2.9: The misfit dislocation network of $Si_{0.8}Ge_{0.2}$ films with different sidewall orientations. (a) is a 150 nm film with < 110 > sidewall orientation. The defect density in selective areas is similar to that in non-selective areas. (b) is a 200 nm film with < 100 > sidewall orientation The selective areas have lower defect densities than non-selective areas, and the < 100 > orientation has fewer defects than the < 110 > orientation despite the greater thickness.

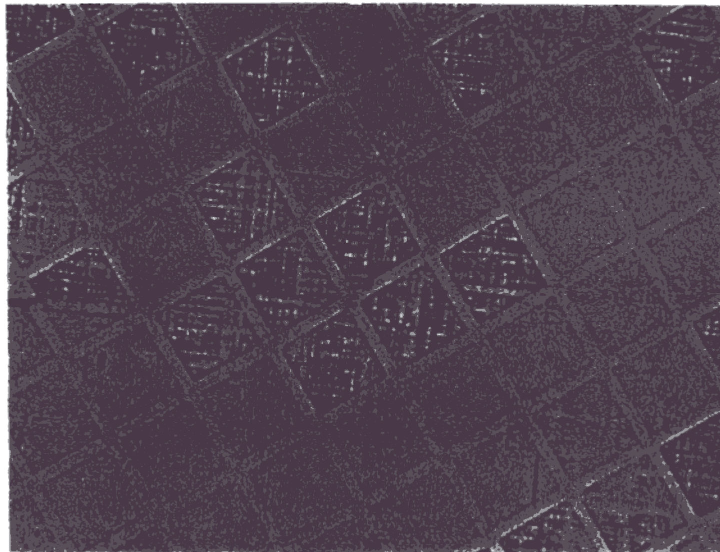

Figure 2.10: Metastability breakdown of selective areas. After 13 hr. annealing at 900°C, some of the selective areas exhibited abnormally large numbers of dislocations, while most other selective areas remained to have relatively small numbers of dislocations.

2.5.3 Summary

A simple model of metastability enhancement for selective $Si_{1-x}Ge_x$ growth has been proposed. From this model, it was found that heterogeneous nucleation at the oxide edge is the dominant source of relaxation in selective areas. The heterogeneous edge nucleation can be controlled by the sidewall orientation of oxide holes.

Chapter 3

Graded Relaxed Buffers for Electron Quantum Devices

3.1 Introduction

The strained-$Si_{1-x}Ge_x$/relaxed-Si material system has been widely investigated for its potential application in heterojunction-based electronic and optoelectronic devices with superior performance over current state-of-the-art silicon devices. Due to the insufficient conduction band offset for this strain configuration, initial devices relied on the valence band offset in strained $Si_{1-x}Ge_x$ layers with respect to relaxed silicon. However, Abstreiter *et al.* [42] then reported successful modulation doping of electrons using a special strain-symmetrized structure. Subsequent experimental and theoretical investigations[29, 43, 13, 44] confirmed that the band alignments depend crucially on the strain configuration and that it was indeed possible to engineer a structure with a significant conduction band offset. This is possible because layers with in-plane tensile strain have their conduction band edges lower than the non-strained adjacent layers. To further illustrate this point, we follow the calculation of van de Walle *et al.* [29] to obtain the band alignments of strained $Si_{1-x}Ge_x$ on various substrates. The results are displayed in Fig. 3.1. The conduction band edges in this figure include 4 Δ-point valleys (perpendicular to growth direction), 2 Δ-point valleys (parallel to growth direction), and 8 L-point valleys, while the valence band edges exhibit heavy

hole, light hole, and split-off hole bands. On Si substrates (Fig. 3.1(a)), the maximum conduction band offset is less than 20 meV for the strained $Si_{1-x}Ge_x$ with $x < 0.5$ (this is the maximum Ge content available in most growth techniques with good material quality). However, on relaxed $Si_{0.6}Ge_{0.4}$ substrates, a conduction band offset as large as 200 meV can be obtained for pure strained Si (type II alignment, lower edge is in Si). Note that the strained SiGe layer with Ge content less than that of the substrate is under tensile strain and the SiGe with Ge content greater than that of the substrate is compressively strained. For strained Si, the conduction band offset between Si and the $Si_{1-x}Ge_x$ substrate increases as the Ge content in the substrates increases.

However, SiGe substrates are not available. Even if available, use of such substrates would remove the advantage of the integration with the Si technology. Therefore, we must grow relaxed SiGe on Si substrates. The thermal equilibrium consideration requires that the $Si_{1-x}Ge_x$ layers grown on Si start to relax only if their thicknesses exceed the critical thicknesses, as discussed in chapter 2.2. The final degree of relaxation depends on layer thickness. Using Matthews and Blakeslee's approach [45], we can obtain relative residual strain (the ratio of vertical strain to the misfit) as a function of the thickness, normalized with the critical thickness (Fig. 3.2), which approximately depends inversely on the thickness. The deviation of relative residual strain from unity is defined as degree of relaxation. For example, 10 % relative residual strain (90 % relaxation) requires a layer thickness of 10 times the critical thickness.

The initial experiment in Ref. [42] used a thick $Si_{0.75}Ge_{0.25}$ buffer layer directly on a silicon substrate to grow modulation doped structures for electrons. It indeed showed the two dimensional electron gas behavior with the peak mobility at low temperature of ~ 2500 $cm^2/V{\cdot}s$. The low mobility was due to the high density of threading dislocations in the conduction channel, which was estimated to be 10^9 –

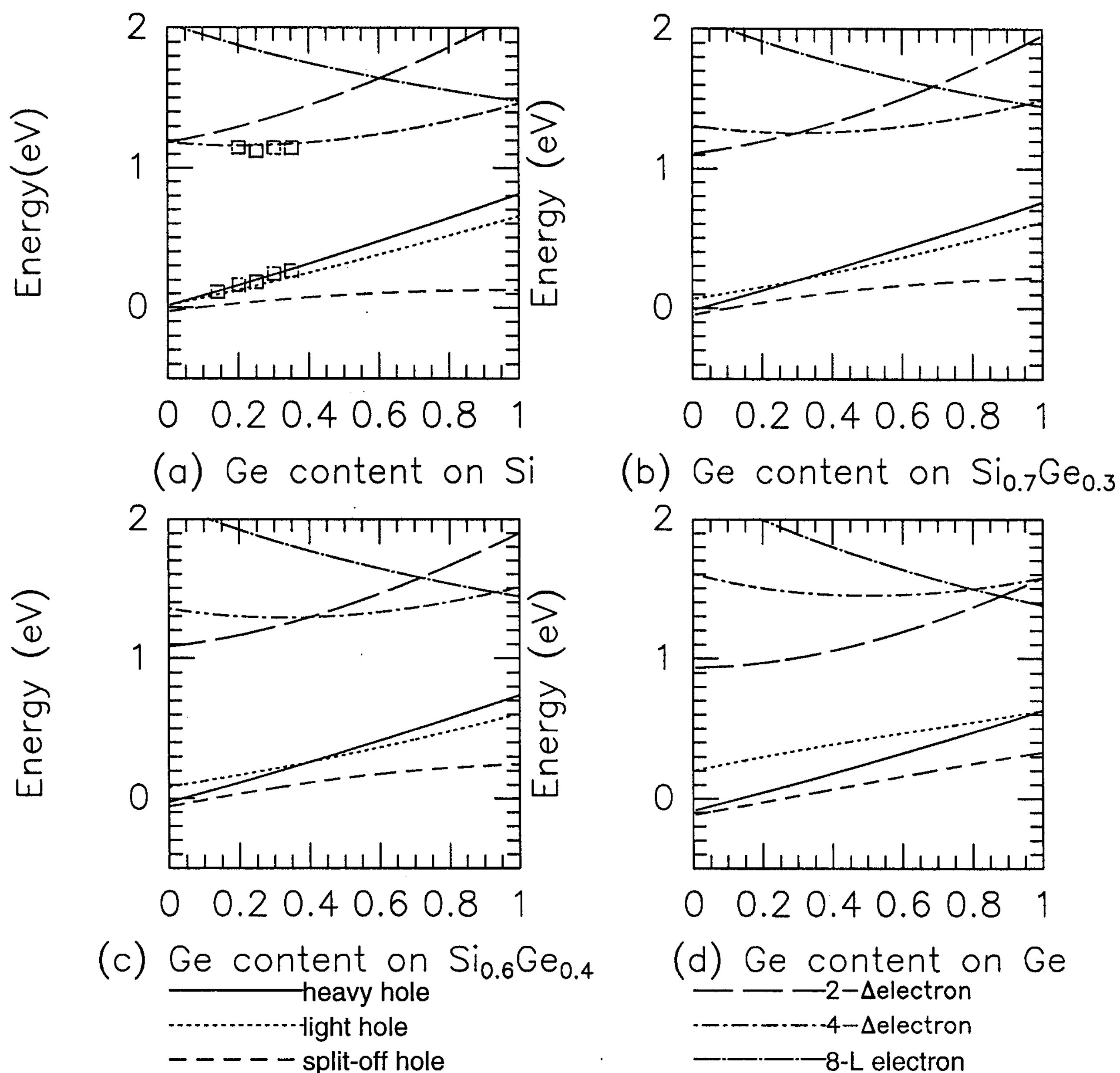

Figure 3.1: Band edge alignments on various SiGe substrates. For strained Si, the conduction band offset between Si and $Si_{1-x}Ge_x$ substrates increases as Ge content in the substrates increases. The data points in (a) are from previous work in our lab [28].

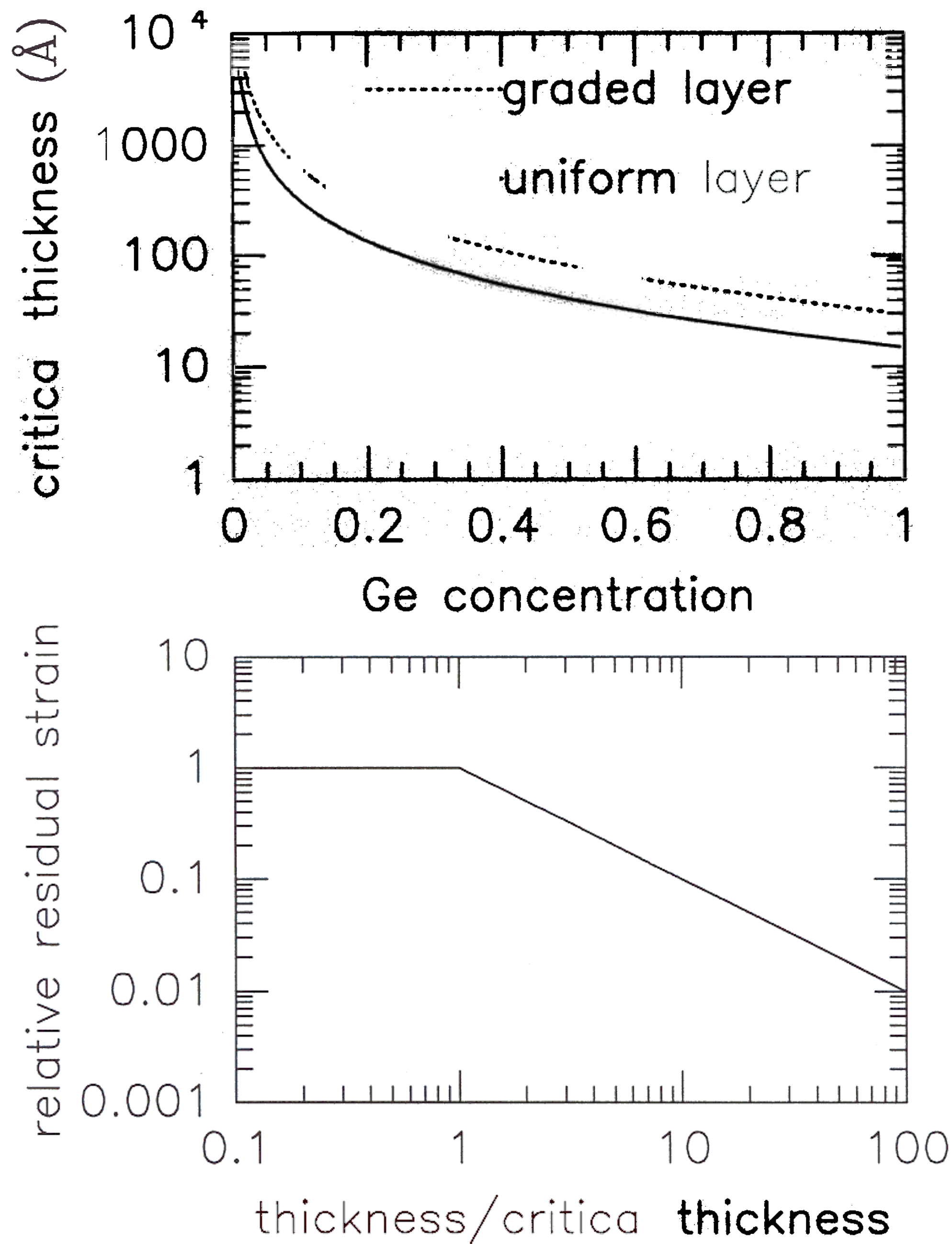

Figure 3.2: Critical thickness versus Ge content and relative residual strain versus thickness normalized with respect to critical thickness. The critical thicknesses of linear graded layers are about two times of thicknesses of uniform layers.

$10^{10}cm^{-2}$ [46]. To further improve the material quality, it is necessary to reduce the threading dislocation density. A clever method (graded relaxed buffer) was used recently to achieve mobilities exceeding 100,000 $cm^2/V \cdot s$ of electrons in the Si channel grown either by UHV-CVD or MBE on silicon substrates [13, 43, 44].

The idea behind the graded relaxed buffer is to avoid the misfit dislocation intersection. It is known that when two misfit dislocations intersect, the intersection often gives rise to a threading segment which goes vertically to the surface [47]. In a graded relaxed buffer, the misfit dislocations are distributed along the graded layer and thus, the probability of intersection is lower, as shown in Fig. 3.3. Note that for uniform buffers, the misfit dislocations are all generated at the interface, so that the rate of intersection to generate threading dislocations is very high. Also note that for a large conduction band offset, a high Ge content and a high degree of relaxation in the relaxed buffer is required. This chapter will focus on the growth and characterization of graded relaxed buffers grown by the RTCVD technique.

In the development of GaAs epitaxial growth, a popular method to reduce the threading dislocation density is to grow strained layer superlattices (SLS's) [48]. In this chapter, the SLS's technique is also studied in the SiGe/Si system.

Finally, we report the electron effective mass measurement of tensilely strained Si and SiGe in the modulation doped structures.

3.2 Growth

The graded relaxed buffer has been previously studied by MBE (molecular beam epitaxy) and UHV-CVD. The growth temperature of MBE samples is relatively high (750-900°C). The advantage of high temperature growth is to promote dislocation propagation, and thus, to ensure sufficient relaxation [47]. In UHV-CVD growth, the growth temperature is relatively low (550°C). Such growth temperature causes

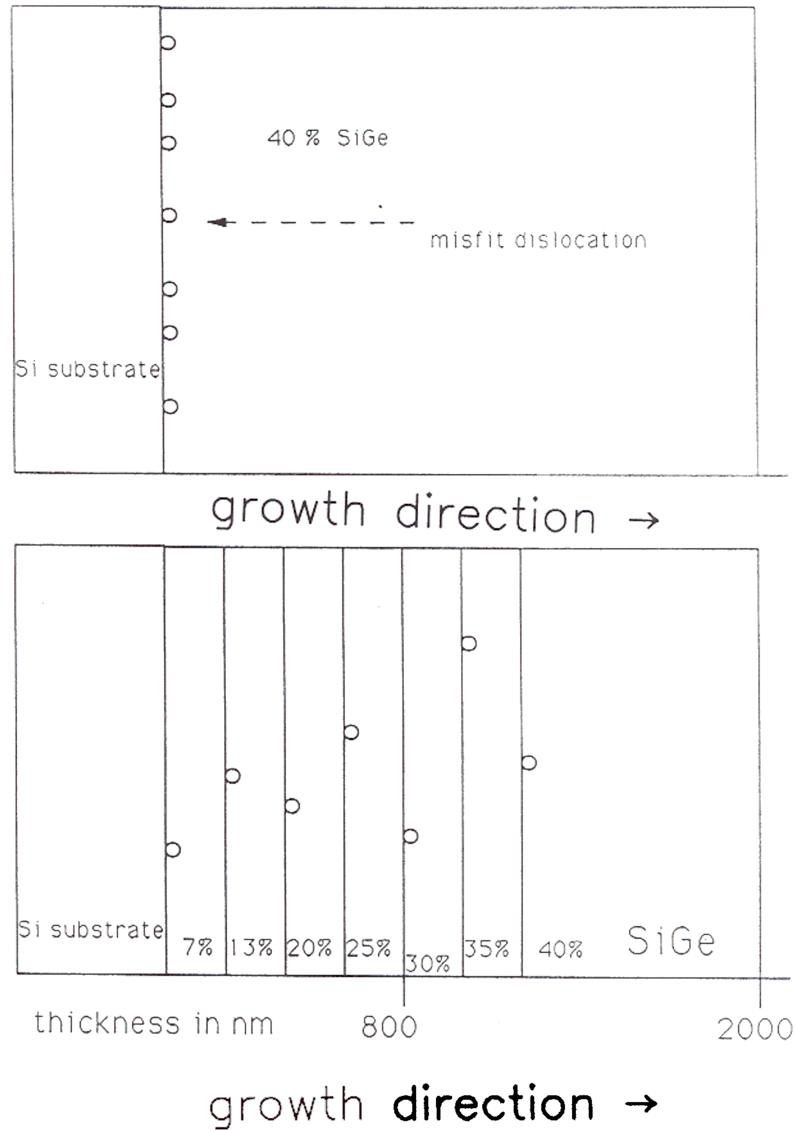

Figure 3.3: Illustration of the graded relaxed buffer to lower dislocation intersection. The intersection process is greatly reduced because misfit dislocations are spatially separated along graded layers.

incomplete relaxation and leads to smaller band offsets and less carrier transfer [44]. In the RTCVD growth of this work, the graded relaxed buffer is grown at 625°C. Although the growth rate is lower, compared to high temperature growth, and the relaxation is not complete, it has the following advantages: (1) The growth data such as growth rate and Ge content (see Chapter 4) are well-established. We can increase the growth time of low Ge content layers, which have low growth rates, to obtain linearly graded buffers. (2) The low temperature can yield higher Ge content in the relaxed buffer at the maximum GeH_4 flow in our reactor, as compared to high temperature growth. This will lead to high electron concentration in modulation doped structures. Our samples have the lowest reported sheet resistance [49] (3) The deposition of SiGe on the quartz tube at high growth temperature and high Ge contamination can be avoided. This allows us to have more repeatable temperature control of different wafers due to the IR transmission temperature measurement in our reactor.

To study the relaxation of the buffers grown by RTCVD, two sets of samples were investigated:

(a) 1 μm thick $Si_{0.52}Ge_{0.48}$ uniform layers were grown on the top of linearly graded layers (0.6 μm) with Ge content from 0% to 48% (sample 836).

(b) 0.6 μm thick $Si_{0.62}Ge_{0.38}$ uniform layers were grown on the top of linearly graded layers (0.5 μm) with Ge content from 0% to 38% (sample 840).

The thickness of uniform layers was measured by the selective etching technique [50] on similar samples without graded buffers. The X-ray diffraction (XRD) spectra of these two samples are shown in Fig. 3.4 for the as-grown films as well as the same samples after 1 hr. annealing at 800°C in nitrogen. For both structures, the (400) peaks of the uniform $Si_{1-x}Ge_x$ layers shifted towards the Si substrate peaks after the samples were annealed at 800 °C for 1 hr., indicating further relaxation. However, if the samples were further annealed for 10 hr. at 800°C, the XRD spectra (not

shown) were similar to those of 1 hr. annealed samples. This indicates that 1 hr. at 800°C was sufficient to relax the as-grown films. The degree of relaxation of these as-grown samples estimated from from XRD was 92% and 88% for $Si_{0.52}Ge_{0.48}$ and $Si_{0.62}Ge_{0.38}$ layers, respectively. The degrees of relaxation are more than 99 % at the thermal equilibrium condition, estimated from Fig.3.2. Note that the double peaks in Fig. 3.4 are due to the $CuK_{\alpha 1}$ and $CuK_{\alpha 2}$ radiation sources. The broad Si peaks in these XRD spectra are due to the instrumental broadening of the powder diffraction machine and become much narrow in the double crystal X-ray rocking curves (see section 6.2). The SiGe peaks have extra broadening due to the high dislocation density. The background between the Si peaks and SiGe peaks is due to the diffraction of the graded layers sandwiched between the Si substrates and the SiGe uniform layers. An interesting feature was that the spectra of annealed samples showed more flat regions between the (400) SiGe peaks and Si peaks, as compared to as-grown samples. This indicates that the annealed samples were more linear in their Ge content than were the as-grown samples. Therefore, the in-situ annealing (1 hr. at 800°C) was adopted in all the relaxed buffer growth. Note that the annealing pressure is 6 torr, which is very important for modulation doped structures, because the sample annealed at 250 torr did not have any two dimensional electron gas.

Auger analysis (Table 3.1, performed by W. D. Chen, Princeton Univ.) of two different samples showed that after annealing at 800°C in vacuum, there was Ge segregation on the surface. After further annealing at 900°C in vacuum, the Ge concentration became much lower at the surface than that of as-grown samples (possibly due to evaporation of Ge atoms).

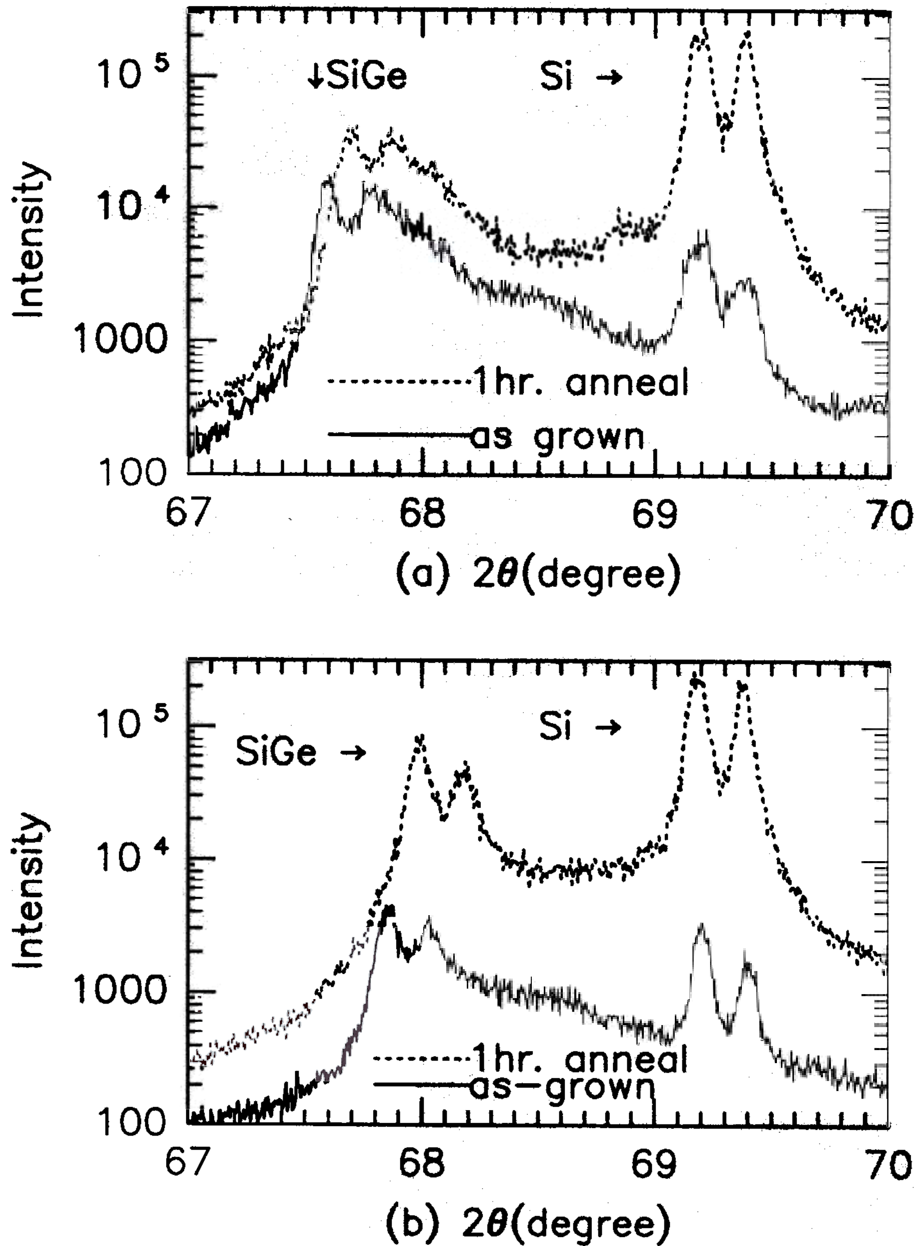

Figure 3.4: XRD spectra of the graded relaxed buffer. (a) are the spectra of a 1 μm thick $Si_{0.52}Ge_{0.48}$ uniform layer grown on the top of linearly graded layers (0.6 μm) with Ge content from 0% to 48% for both as-grown samples and 1 hr. 800°C annealed samples. (b) are the spectra of a 0.6 μm thick $Si_{0.62}Ge_{0.38}$ uniform layer grown on the top of linearly graded layers (0.5 μm) with Ge content from 0% to 38% for both as-grown samples and 1 hr. 800°C annealed samples. From the shifts of (400) SiGe peaks, we can estimate that the degrees of relaxation of these as-grown samples were 92% and 88% for $Si_{0.52}Ge_{0.48}$ and $Si_{0.62}Ge_{0.38}$ layers, respectively.

Sample	annealing condition	Ge(1147eV)/Si(1619eV)	comment
976 ($Si_{0.3}Ge_{0.7}$)	as-grown	2.9	–
976	800°C 20 min.	4	segregation
976	900°C 30 min.	2	evaporation
966 ($Si_{0.62}Ge_{0.38}$)	as-grown	4.7	–
966	800°C 5 min.	5	segregation
966	900°C 2 min.	4	evaporation

Table 3.1: Auger analysis of samples at different annealing conditions. Ge/Si is the Auger signal ratio of Ge (1147eV) to Si (1619). The compositions of top uniform layers are indicated in column I. 800 °C anneal showed evidence of Ge segregation. 900 °C anneal showed evidence of Ge evaporation.

3.3 Characterization

Transmission electron microscopy (TEM, performed by Dr. J. T. McGinn of the David Sarnoff Research Center) was utilized to study the defect density and structure of the graded relaxed buffers with uniform layers. The cross section TEM of the 38% Ge sample (sample 892, in-situ annealed at 800 °C for 1 hr after a uniform layer was deposited) is shown in Fig. 3.5. Most dislocations were confined in the graded layers, and relatively few dislocations threaded toward the surface. Some dislocations, most surprisingly, penetrated deep into Si substrates. This is contradictory to Matthews and Blakeslee's theory, in which they assumed the dislocations were always confined to the epilayers, because of the relatively small thickness of the epilayers as compared to substrates. A modified Frank-Read source was proposed to explain this phenomenon which was also observed in similar structures grown by UHV/CVD [51]. In this model, a dislocation segment pinned at two ends can bow out under the shear stress, and finally form a complete loop with the initial segment, but no general agreement is reached. In any case, it is clear that the graded relaxed buffer successfully reduces the density of the threading dislocations at the surface.

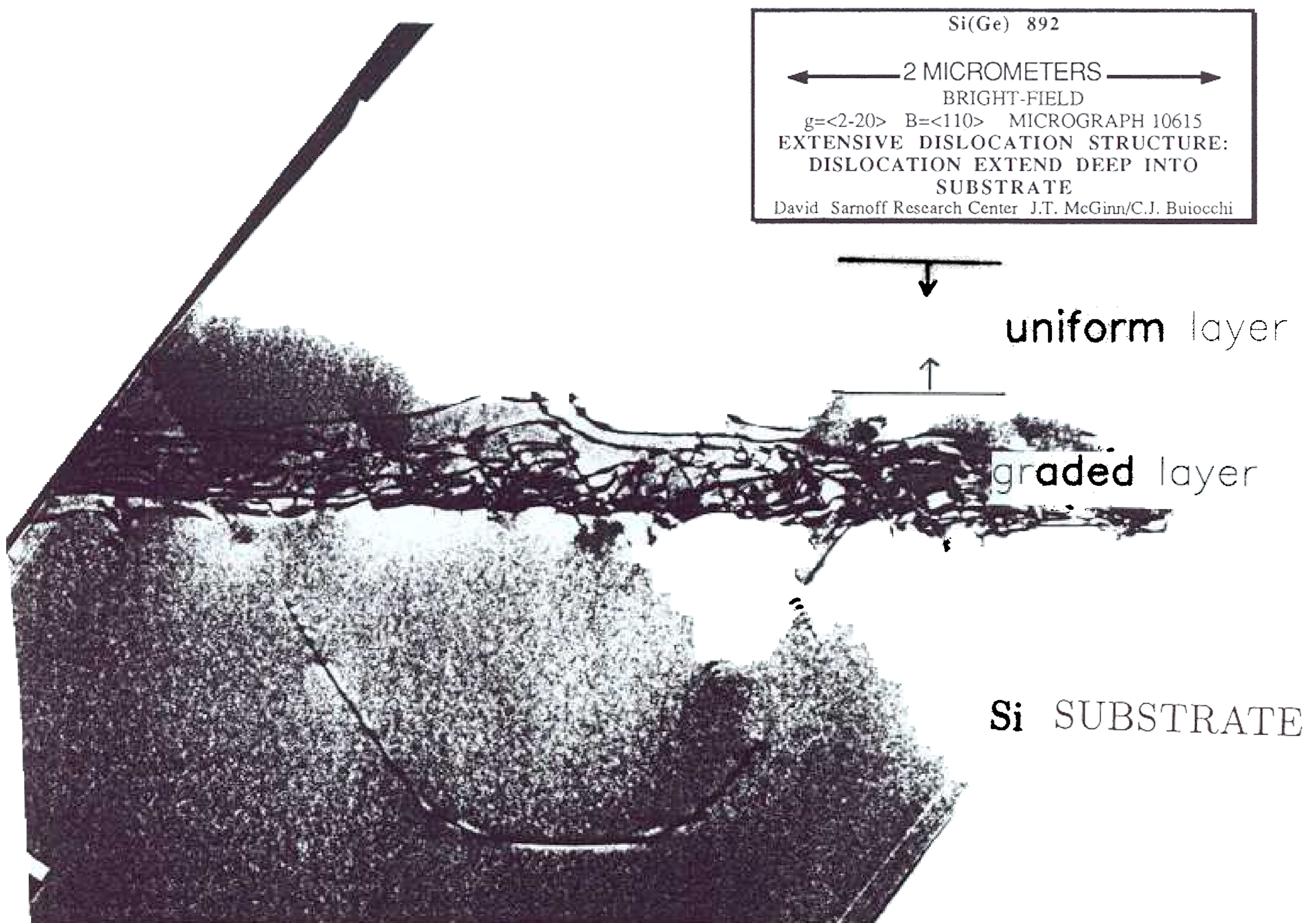

Figure 3.5: XTEM picture of graded relaxed buffers. Most dislocation networks were confined in the graded layers and relatively few dislocations threaded toward the surface. Some dislocations, most surprisingly, penetrated deep into Si substrates.

The surface morphology of the graded relaxed buffers is very rough, however. The roughness of similar graded buffers (b) has been studied by Nomarski microscope and atomic force microscope (AFM). The roughness revealed cross hatched patterns and had a rms value of 46 Å (sample 910), averaged over a 30x30 μm^2 area, which was consistent with the prediction of Ref. [52].

To study the threading dislocation density quantitatively, plan-view TEM and electron beam induced current (EBIC) imaging were obtained. The plan-view pictures of a sample (sample 975) similar to sample 892 are shown in Fig. 3.6 and Fig. 3.7 for two different regions of the same sample. The threading defects were not distributed uniformly within the same sample, and "defect bands" existed at the surface. In the bands, the defect density was about 10^8 cm^{-2} (Fig. 3.6). Outside the bands, the defect density was remarkably reduced to about $5x10^6 cm^{-2}$(Fig. 3.7). The band to band spacing was more than 10 μm, and a typical bandwidth was 1-3 μm.

Because dislocation densities measured with TEM are very inaccurate at these low dislocation densities, we recorded EBIC images from a relaxed buffer (sample 892) with extra p-n junction near the surface. Assuming that the threading defects serve as recombination centers either through their intrinsic properties or due to metal impurity decoration, one can see the effect of dislocations on the minority carrier current. An electron beam energy of 10-20 KeV was used. The resolution of EBIC tends to smear out the detailed feature of threading defects as observed in TEM, and therefore the image of a threading defect in EBIC is presumably a dot. A typical EBIC image of a graded relaxed buffer is displayed in Fig. 3.8. The defect bands were not observed by EBIC, probably due to the low resolution of EBIC. From the picture, the dislocation density is determined to be $\sim 3 \times 10^7$ cm^{-2}. From the threading dislocation density, we can estimate the misfit dislocation length by the equation in Ref. [47].

$$L \quad 8(\frac{f}{\rho})b \tag{3.1}$$

where ρ is the threading dislocation density. The misfit dislocation length is about 0.14 cm.

To further reduce the threading dislocation density, we have to increase the misfit dislocation length. In the next section, strained layer superlattices were used to deflect the threading segments either to move towards the sample edge or to annihilate after encountering another dislocation with the same Burger's vector [53]. Note that either way will increase the misfit dislocation length, and thus decrease the threading dislocation density.

Figure 3.6: plan-view TEM picture of graded relaxed buffer. In this area, a defect band existed. The defect density in the band was about 10^8 cm^{-2}.

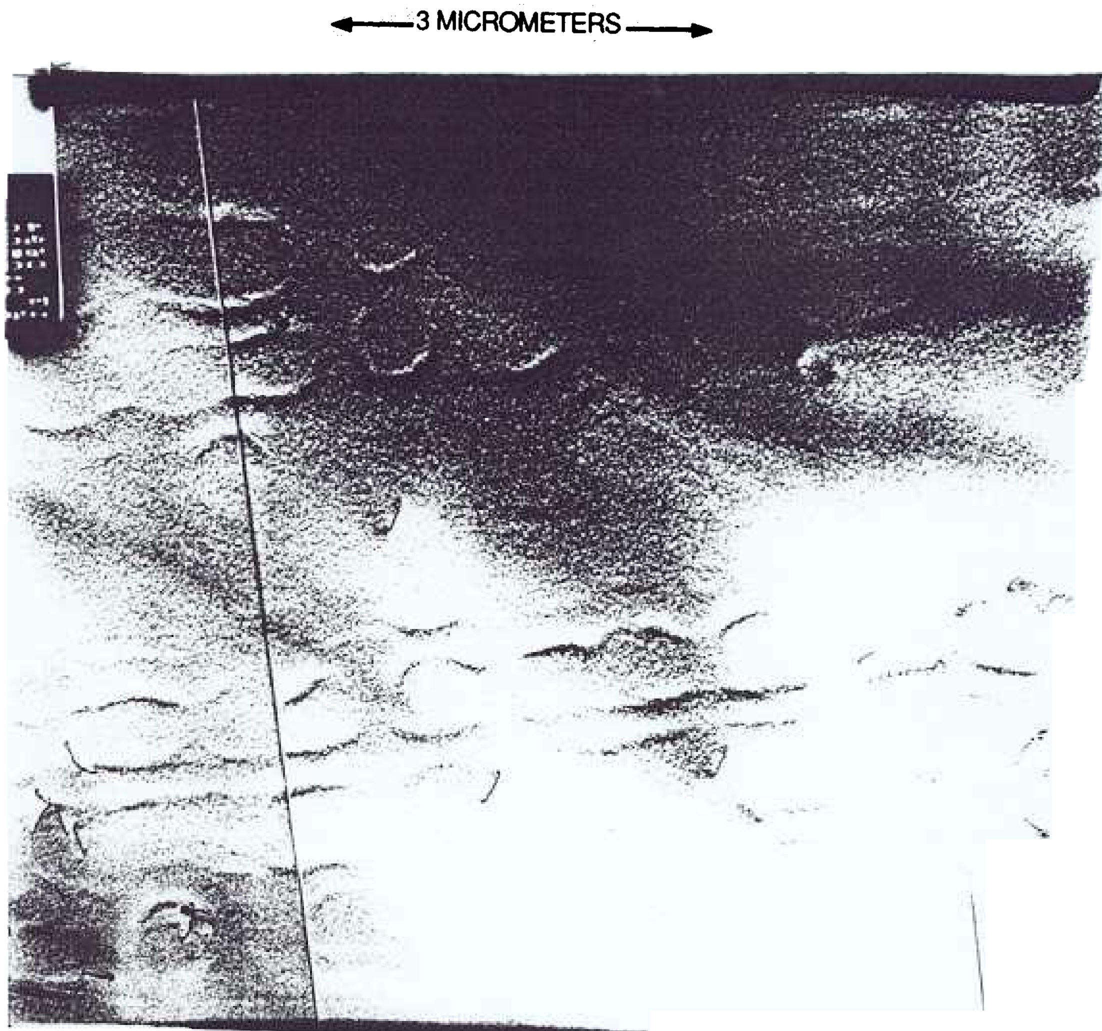

Figure 3.7: plan-view TEM picture of graded relaxed buffer. In this area, no defect band existed. The defect density was about 5x10^6 cm^{-2}.

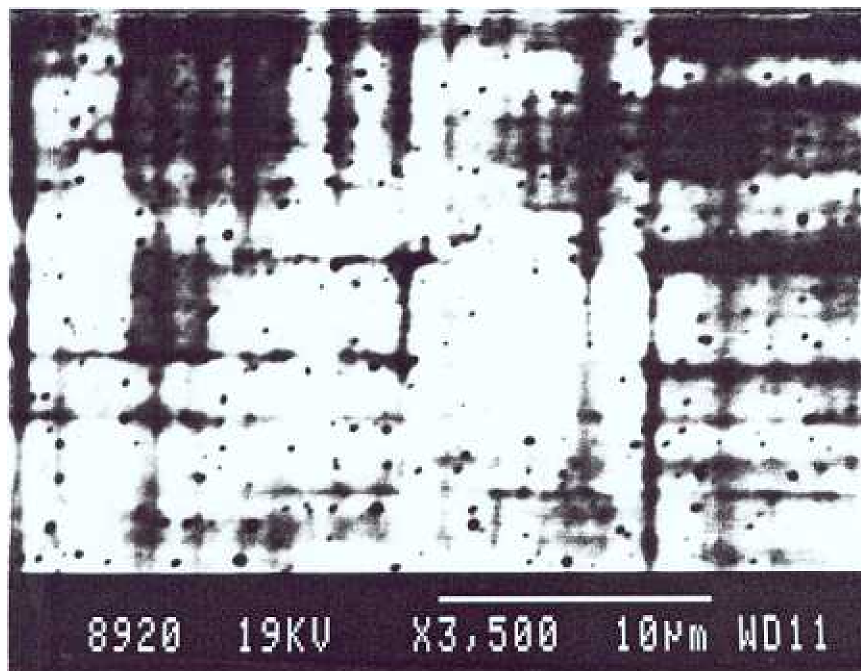

Figure 3.8: Electron Beam Induced Current (EBIC) image of a graded relaxed buffer. Assuming the dark spots were threading dislocations, we inferred a dislocation density of $\sim 3 \times 10^7$ cm^{-2}.

Strained layer superlattices

One possible mechanism for reducing the threading dislocation density is to grow strained layer superlattices (SLS's) on top of defective layers. If the strain at the interface is of sufficient magnitude, the SLS's might push two threading segments toward each other. Hopefully, the two threading segments might annihilate. However, the thickness of the SLS's should be less than the critical thicknesses of the whole layer and so is each individual layer. This will prevent extra dislocation generation. To follow the constraints of the SLS's, we designed 2 sets of samples, one (sample 976) with and one (sample 975) without SLS's on the top of graded relaxed buffers. The graded relaxed buffers consisted of 0.7 μm $Si_{0.7}Ge_{0.3}$ uniform layers on the graded layers with Ge content from 0% to 30% (0.4 μm). The SLS's had 40 periods of 40Å $Si_{0.62}Ge_{0.38}$ and 20Å $Si_{0.8}Ge_{0.2}$ with a total thickness of 2400Å and a slightly net positive strain of 0.008, compared to the relaxed $Si_{0.7}Ge_{0.3}$ buffer. From extensive plan-view TEM study (surveying a large area on the samples), the SLS's can reduce the threading dislocation density by a factor of about 3. Although the density obtained by plan-view TEM was not very accurate, the XTEM indeed showed that the threading dislocations were deflected along the interface (Fig. 3.9). A close up view of SLS's is shown in Fig. 3.10, and no defects appear in this micrograph.

The limited reduction of the threading dislocation density probably has two reans:

(1) To escape at the edge of the wafer, the misfit segment must travel a long distance. This will encourage the dislocation multiplication and the formation of extra threading dislocations.

(2) The annihilation process has a relatively low probability compared to multiplication.

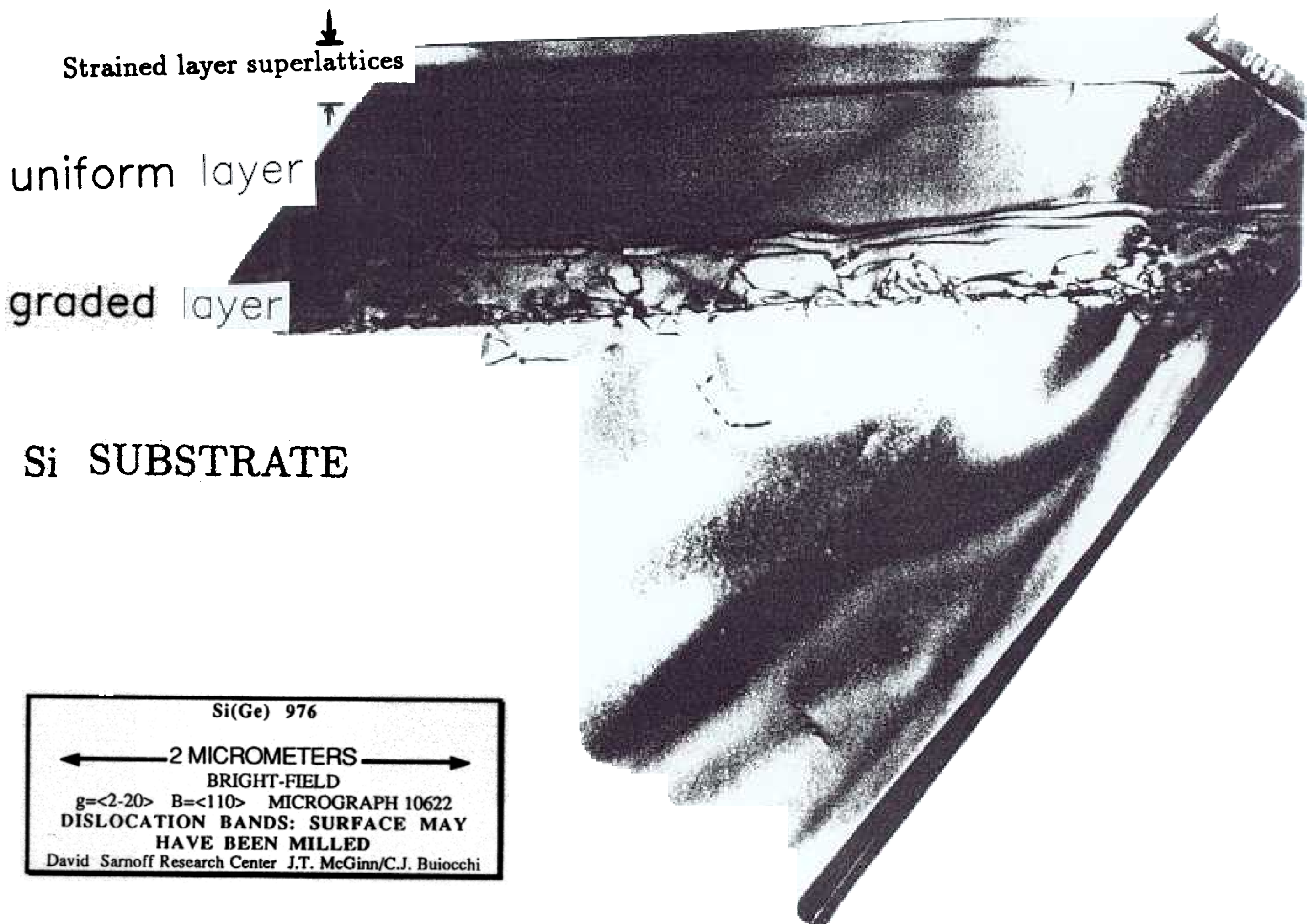

Figure 3.9: XTEM image of SLS's on the relaxed buffer. The graded relaxed buffer consisted of 0.7 μm $Si_{0.7}Ge_{0.3}$ uniform layers on the graded layers with Ge content from 0% to 30%. The SLS's had 40 periods of 40Å $Si_{0.62}Ge_{0.38}$ and 20Å $Si_{0.8}Ge_{0.2}$ with a total thickness of 2400Å and a slightly net positive strain of 0.008, compared to the relaxed $Si_{0.7}Ge_{0.3}$ buffer.

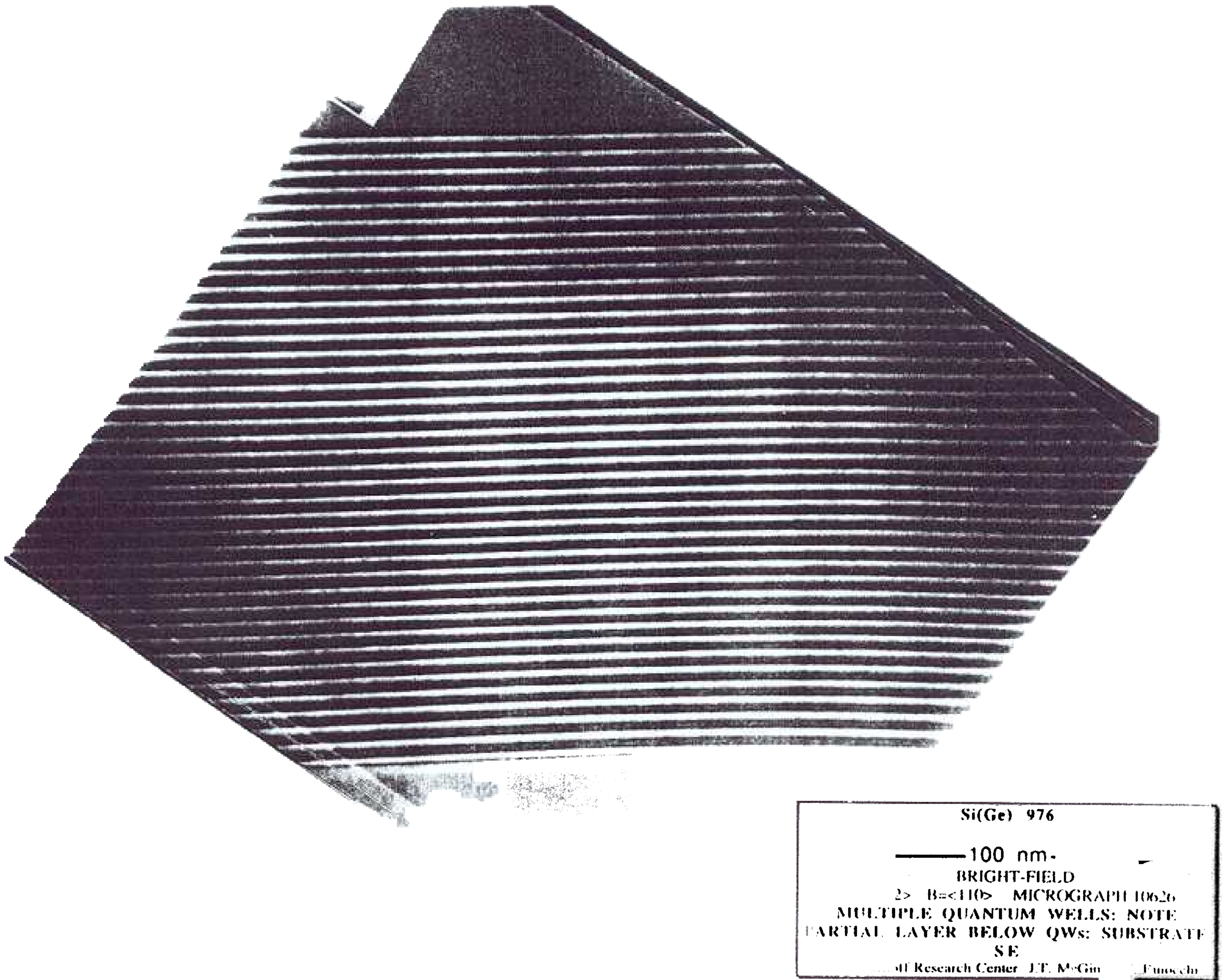

Figure 3.10: High resolution XTEM image of SLS's on the relaxed buffer. No defect was observed in this micrograph.

3.5 Device applications and effective mass measurement

The high quality material of the graded relaxed buffer was used to fabricate electron resonant tunneling diodes and the two dimensional electron gases in the modulation doped structures with very successful results. The results of the electron resonant tunneling diodes were given in Ref. [9, 54] and will be presented in the thesis of Z. Matutinovic-Krstelj. The results of modulation doped two dimensional electron gas were reported in Ref. [55, 56] and in the thesis of V. Venkataraman [36]. The standard structure of a graded relaxed buffer consisted a 0.5 μm graded layer for Ge content from 0 % to 38 % and a 0.6 μm uniform $Si_{0.62}Ge_{0.28}$. This structure was then in-situ annealed at 800 °C for 1 hr at 6 torr in hydrogrn.

Here, we only report the effective mass measurement (by electron cyclotron resonance) of tensilely strained Si (sample 1341) and $Si_{0.94}Ge_{0.06}$ (sample 1381) layers in modulation-doped structures on $Si_{0.62}Ge_{0.38}$ graded relaxed buffers as shown in Fig. 3.11. The effective mass results of these two samples are summarized in Table 3.2 as well as the carrier density (n) and the mobility (μ). For comparison, the results in Ref. [57] are also included.

The cyclotron resonance spectra (obtained by Dr. S. H. Song, Princeton University) of each sample are shown in Fig 3.12(a) and Fig 3.12(b) for the Si channel and the $Si_{0.94}Ge_{0.06}$ channel, respectively. The effective mass values were then extracted from the positions of absorption peaks, using the equation of cyclotron resonance [58]

$$2\pi c\bar{\lambda} = eB/m^* \tag{3.2}$$

where the $\bar{\lambda}$ is the wavenumber, c is the speed of light, e is the electron charge, B is the magnetic field, and m^* is the effective mass. As a result, the effective mass, $0.20m_o$, of tensile Si was very close to the value of 0.195 m_o of tensile Si on relaxed $Si_{0.7}Ge_{0.3}$ buffers reported in literature [57].

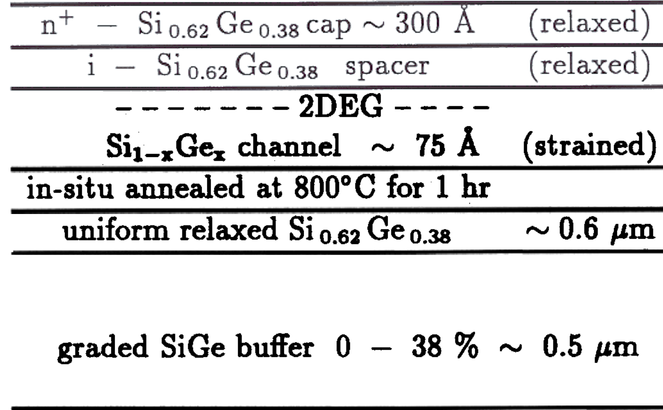

Figure 3.11: Sample structure for effective mass measurement. The samples had 100Å spacers and $\sim 2 \times 10^{19}$ cm^{-3} n-type caps with $Si_{1-x}Ge_x$ channels (0% or 6%) grown at 625 °C.

Sample	x	n(10^{11} cm^{-2})	μ(cm^2/Vs)	$m_{eff}(m_o)$	buffer composition
1341	0.00	12.0	20 000	0.20	$Si_{0.62}Ge_{0.38}$
1381	0.06	14.0	6 420	0.19	$Si_{0.62}Ge_{0.38}$
Ref. [57]	0	4.1	111 000	0.195±0.004	$Si_{0.70}Ge_{0.30}$

Table 3.2: Summary of effective mass results of tensile strained Si and $Si_{0.94}Ge_{0.06}$ channels as well as the two dimensional electron concentrations and mobility at 4.2K.

The striking result is that the effective mass of tensile $Si_{0.94}Ge_{0.06}$ (0.19 m_o) is lower than that of tensile Si, while the effective mass of bulk Ge at Δ points is 0.29m_o higher than that of bulk Si (0.19 m_o). Further work is necessary to confirm the results and to establish error bars on the measurements.

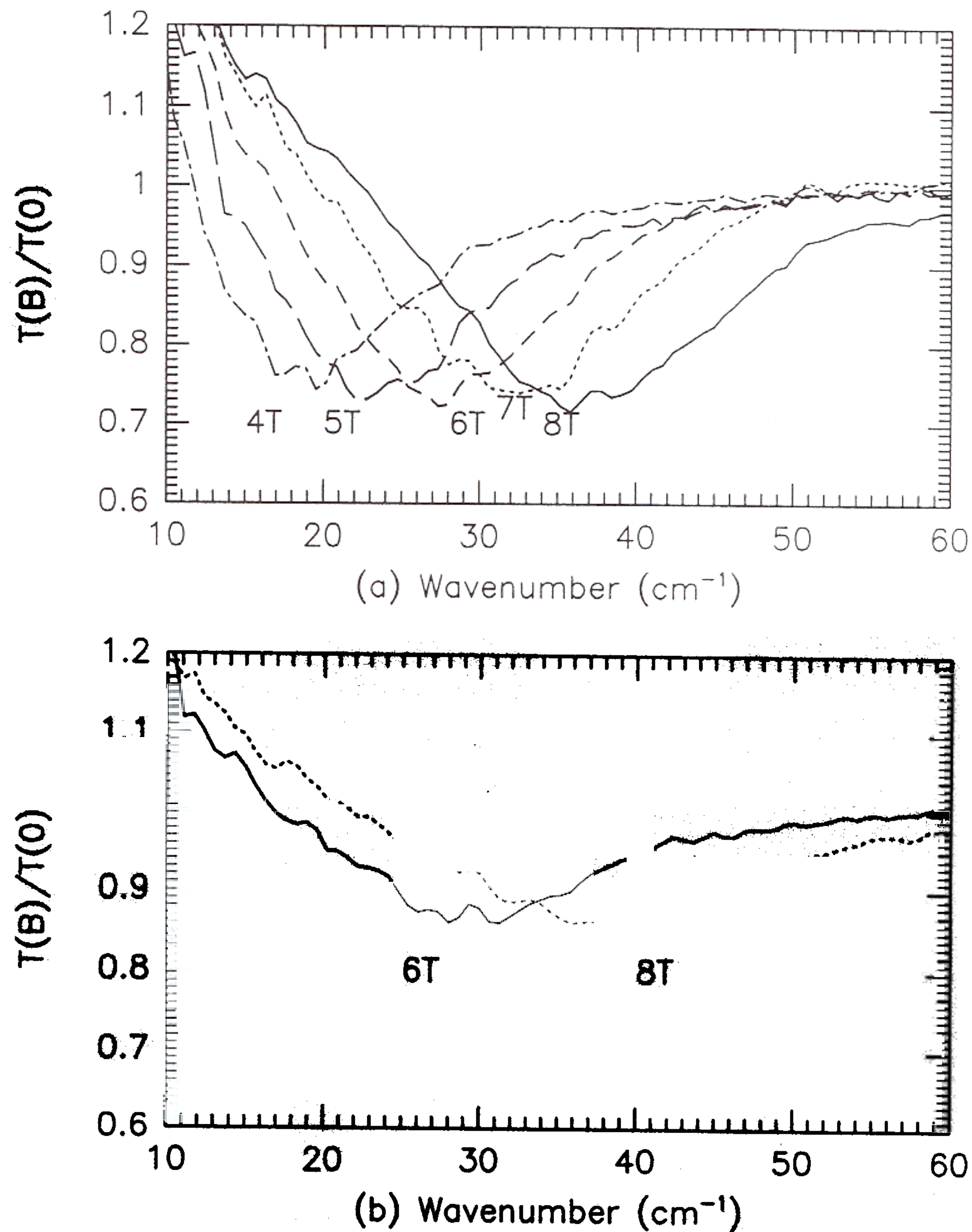

Figure 3.12: The normalized cyclotron resonance spectra at 4.2K for applied magnetic field as labeled. (a) and (b) are for Si channel and $Si_{0.94}Ge_{0.06}$ channel, respectively.

Chapter 4

Growth and Photoluminescence of Strained SiGe on < 110 > Si

4.1 Introduction

The growth and optical properties of $Si_{1-x}Ge_x$ on Si $< 100 >$ oriented substrates have been widely studied, but little work has been done on other substrate orientations. In this chapter, we report the first chemical vapor deposition (RTCVD) growth of $Si_{1-x}Ge_x$ alloys on $< 110 >$ silicon substrates and a photoluminescence study of such alloys in quantum well structures. The $< 110 >$ strained $Si_{1-x}Ge_x$/Si heterojunction is of great interest because the orientation of strain can dramatically change the conduction band minima of strained $Si_{1-x}Ge_x$ on Si (which do not lie at the Γ point) For example, on $< 100 >$ Si substrates, four conduction band minima of strained $Si_{1-x}Ge_x$ move down in energy and two move up; on $< 110 >$ substrates the opposite is predicted. On $< 111 >$ substrates, the six conduction band minima are predicted to remain degenerate. Moreover, the $< 110 >$ substrate has the largest predicted conduction band offset (for type I alignment) between strained $Si_{1-x}Ge_x$ and Si among these three substrate orientations [29].

The bandgap of strained $Si_{1-x}Ge_x$ on $< 100 >$ Si was measured by Lang *et al.* [59] by photocurrent measurements. In this study, we use photoluminescence to measure the bandgap of strained $Si_{1-x}Ge_x$ on $< 110 >$ Si substrates. Using the no-phonon

(NP) process (momentum conserved by lattice disorder in the indirect bandgap material), we can accurately determine the the bandgap without correcting for phonon energy. The dependence of the no-phonon luminescence process on quantum well width is then used to perform the first measurement of the conduction band offset in

110 > quantum well structures.

Growth

The < 110 > samples studied by previous work were all grown by molecular beam epitaxy (MBE). These include a dislocation study [60], electron intersubband transition [61], and one photoluminescence report of a single sample [62]. All samples reported in this chapter were grown by RTCVD on 100 mm wafers (except sample 1361 on a 75 mm wafer). The Si layers were grown at a nominal temperature of 700 °C from dichlorosilane (DCS), and the $Si_{1-x}Ge_x$ layers were grown at a nominal temperature of 625 °C from germane and DCS. An anomalously low growth temperature on sample 1361 may explain unexpectedly large Ge fraction (43 %) on that sample. The growth pressure was 6 torr, the gas flows were 3 slpm for a hydrogen carrier and 26 sccm for dichlorosilane, and the germane mixture flow (0.8 % in hydrogen) varied from 100 to 450 sccm. For samples characterized by photoluminescence, the $Si_{1-x}Ge_x$ layers were capped with ~ 100Å of silicon, because previous experiments on < 100 > samples in our lab have shown that a Si cap increases the photoluminescence intensity by over an order of magnitude, presumably due to a decrease in surface recombination [63]

The thickness of $Si_{1-x}Ge_x$ quantum well samples were measured by cross-sectional transmission electron microscopy (XTEM, performed by Prof. D. D. Perovic of Univ. of Toronto). The strained $Si_{1-x}Ge_x$ layers were observed by XTEM to be abrupt within 0.3-0.4 nm, similar to < 100 > layers of similar thickness grown either by

sample #	thickness(Å)	x	$E_{g,PL}$ (eV)	r_{np}	ΔE_{conf} (eV)	E_g(eV)
1361	23 ± 3	0.43 ± 0.08	0.947 ± 0.005	2.66	0.110 ± 0.029	0.837 ± 0.029
1463	51 ± 3	0.29 ± 0.02	0.916 ± 0.005	3.15	0.059 ± 0.007	0.857 ± 0.009
1464	62 ± 4	0.26 ± 0.02	0.957 ± 0.005	2.06	0.041 ± 0.005	0.916 ± 0.007
1465	127 ± 4	0.21 ± 0.01	0.973 ± 0.005	1.51	0.013 ± 0.001	0.96 ± 0.005
1466	106 ± 4	0.16 ± 0.01	1.017 ± 0.005	1.0	0.016 ± 0.002	1.001 ± 0.005

Table 4.1: Summary of the quantum well samples used in the study. The thickness is measured from cross-sectional TEM. The Ge composition(x) is determined by the combination of cross-sectional TEM and RBS. $E_{g,PL}$ and r_{np} are obtained from photoluminescence. The quantum confinement energy (ΔE_{conf}) is calculated from the conditions of a square potential profile, a theoretical valence band discontinuity $\Delta E_v = 0.71x$ [29], the measured quantum well thickness, the hole effective mass of 0.28 m_o [64], and the electron effective mass of 0.19 m_o. The E_g is the bandgap after quantum confinement corrections. The uncertainty in $E_{g,PL}$ is from fitting the PL spectra, and the uncertainty in ΔE_{conf} is from the uncertainty in the quantum well thickness.

CVD or MBE techniques. Moreover, all of the quantum wells were defect-free on the scale of XTEM. Rutherford Backscattering Spectroscopy (RBS) was performed by Dr. H. Gossmann of ATT Bell Labs to find the integrated atomic areal density. Using the thickness from XTEM and Ge areal density from RBS, and assuming that atomic density of $Si_{1-x}Ge_x$ is a linear function of Ge content, and abrupt interfaces, we obtained the Ge content in the quantum wells. The measured Ge content and quantum well thickness of each sample is summarized in Table 4.2

The growth rate and Ge content vs germane mixture flow are plotted in Fig. 4.1 and Fig. 4.2, respectively, with the results on < 100 > substrates.

Both the Ge content and the growth rate increase as germane flow increases. Compared to < 100 > Si substrates, the same growth conditions yielded $Si_{1-x}Ge_x$ layers with a slightly lower Ge content, but much lower growth rates (a factor of 2-3 lower).

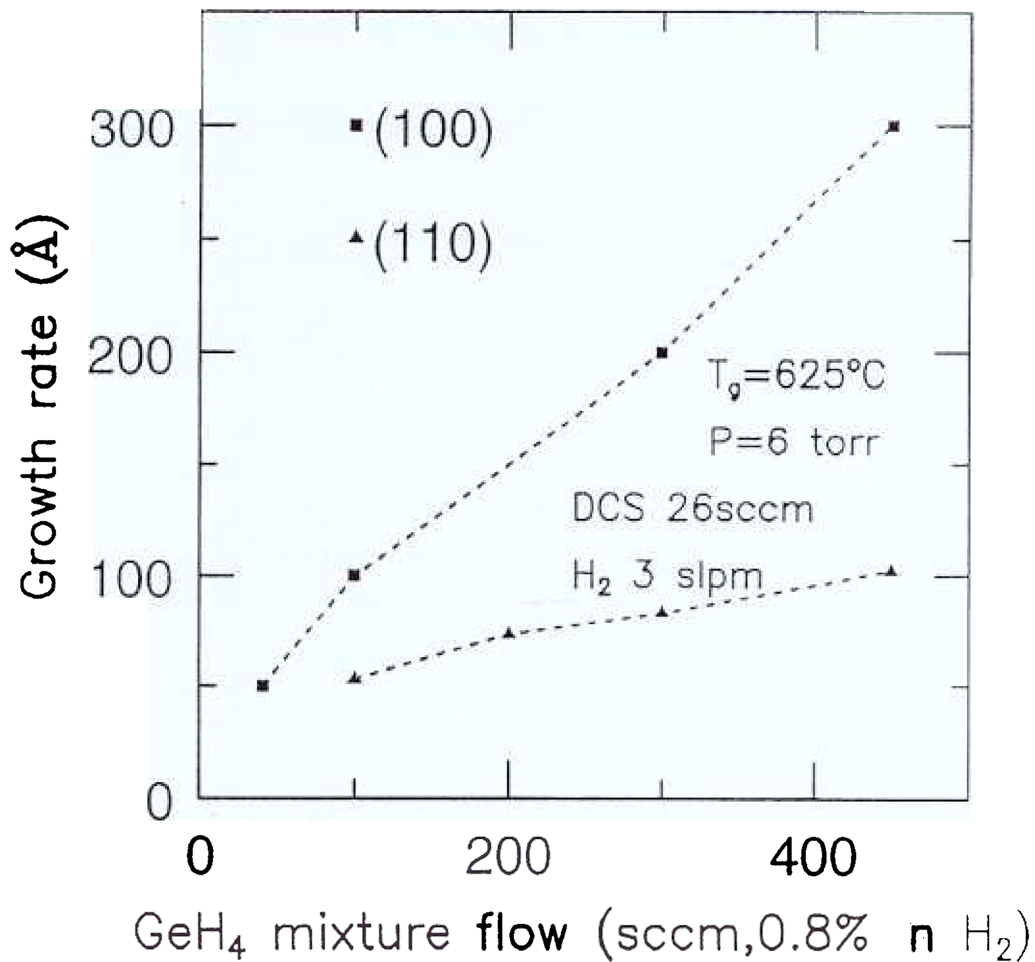

Figure 4.1: Growth rate of SiGe vs germane flow(sample 1463-1466). Compared to (100) Si, the growth rate on (110) Si is lower by a factor of 2-3. The growth temperature was 625 °C and the pressure was 6 torr with 26 sccm dichlorosilane and 3 slpm hydrogen flows.

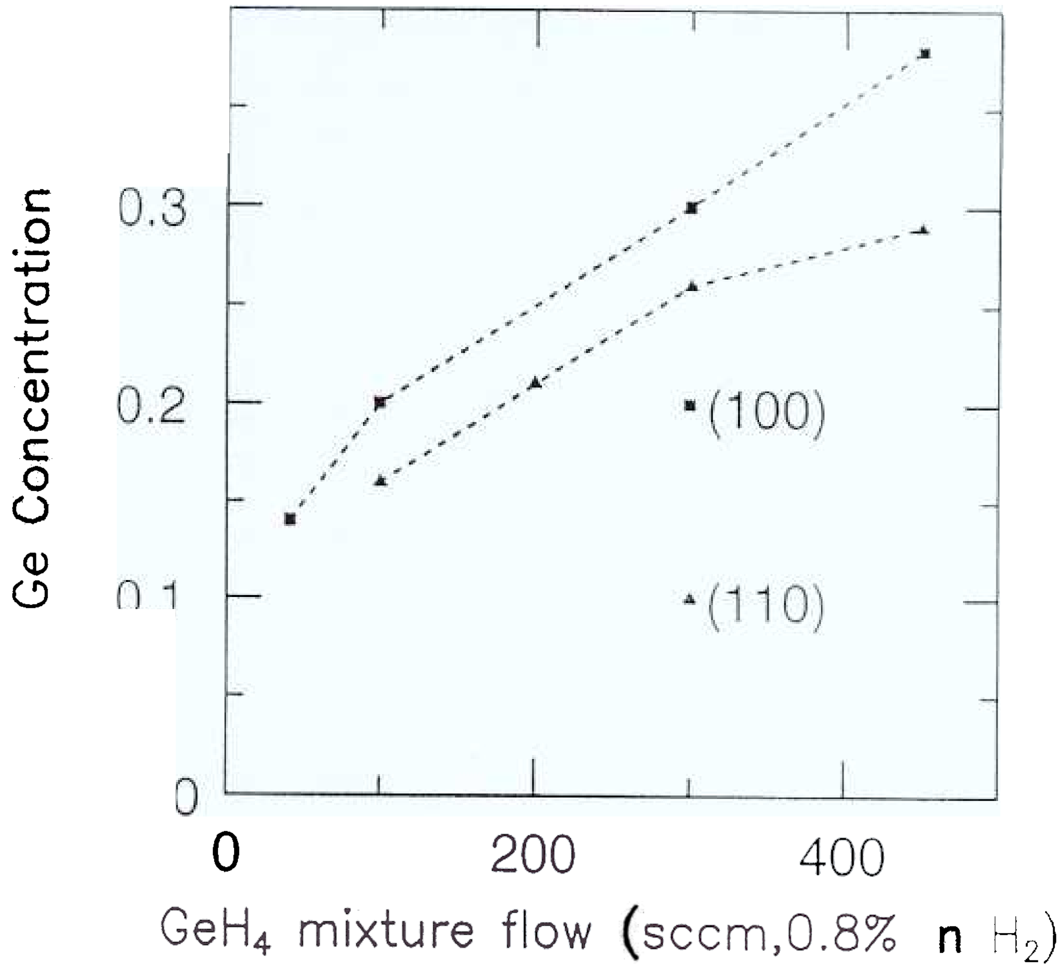

Figure 4.2: Ge content of SiGe vs germane flow. Compared to (100) Si, the Ge content of SiGe on (110) Si is slightly lower. The growth temperature was 625 °C and the pressure was 6 torr with 26 sccm dichlorosilane and 3 slpm hydrogen flows.

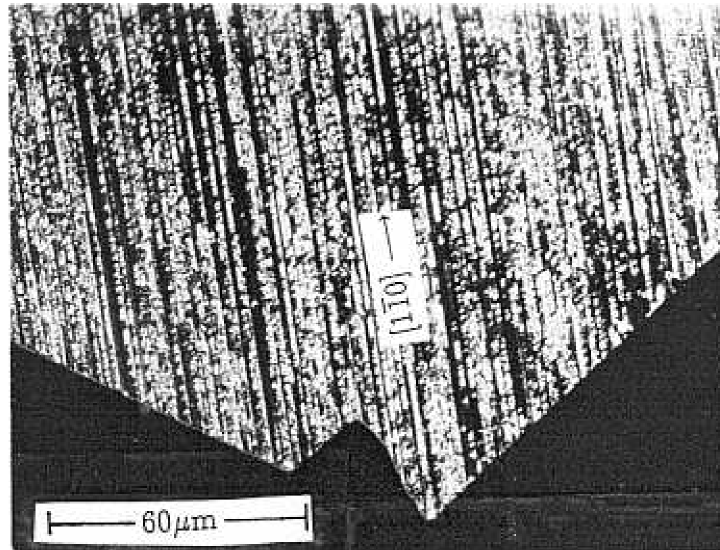

Figure 4.3: The Nomarski micrograph of a 0.5μm $Si_{0.71}Ge_{0.29}$ relaxed layer. cations along only one direction were observed.

To study the relaxation of the SiGe films on $< 110 >$ Si, we investigated the morphology and the X-ray diffraction (XRD) on thick layers ($\geq 0.5\mu m$) grown under the same conditions as the quantum well samples and annealed at 900°C for 3 hr. to promote relaxation. The plane-view Nomarski micrographs (Fig.4.3) of the thick (110) $Si_{1-x}Ge_x$ films revealed only one set of dislocation lines, which were along the [001] direction (the dislocation line parallel to $[1\bar{1}0]$ direction), indicating that the relaxation on the orthogonal $[1\bar{1}0]$ direction was retarded.

Furthermore, the vertical lattice constants measured from (440) peaks of XRD spectra of $Si_{1-x}Ge_x$ for different Ge contents (x determined from quantum well samples) are systematically 1.1 – 1.2 times larger than the fully relaxed lattice constants. The theoretical ratios of the vertical lattice constant to the relaxed one calculated from elasticity theory are 1.5 and 1.18 for the fully biaxial strained lattice and the fully uniaxial strained lattice (along $[1\bar{1}0]$), respectively (see section 2.2). This fur-

ther confirms the relaxation is predominantly uniaxial on thick $Si_{1-x}Ge_x$ layers grown on Si. Similar results have been observed on MBE samples [60]. This effect is because only two inclined (111) glide planes which can contribute relaxation among the four equivalent (111) planes intersect the (110) growth plane and both intersections (i.e., dislocation lines) are along the same direction [60]. The other two (111) planes are perpendicular to the growth plane and their Burger's vectors (which lies in the glide planes) perpendicular to the normal of dislocation lines (if any) can not cause relaxation, i.e., the $cos\lambda$ is zero in Eqn. 2.7.

Photoluminescence and bandgap

The 4K and 77K photoluminescence (PL) were taken with samples immersed in liquid helium and liquid nitrogen, respectively. The excitation source was an Ar^+ ion laser. All the samples in the PL measurement were quantum well structures. The 4K PL was performed by Y. Lacroix and M. Thewalt of Simon Fraser Univ. At 4K, the PL spectrum of a 23 Å strained < 110 > $Si/Si_{.57}Ge_{.43}/Si$ quantum well (Fig. 4.4(a)) is qualitatively similar to what has been reported in < 100 > substrates [35, 65], and presumably due to shallow bound exciton recombination from band edges. The strongest peak in the spectrum is the no-phonon (NP) transition due to the lattice disorder (mainly alloy fluctuations) which relaxes the momentum conservation requirement. Similar to that observed in < 100 > wells, there are four phonon-assisted replicas at the lower energy side of the NP line, which are attributed to the transverse acoustical (TA) phonon and the three transverse optical (TO) phonon replicas related to Si-Si, Si-Ge, and Ge-Ge vibrations. Only a few of the quantum wells exhibited such strong well-resolved band-edge luminescence at 4K, while all of them exhibited band-edge luminescence at 77K. The reason for this effect is not clear, but may be related to nonradiative traps due to an intermittent vacuum integrity or gas purity

problem in the CVD reactor. These nonradiative traps might introduce scattering of carriers and prevent the carriers generated in Si barriers from reaching the SiGe wells at low temperature (low thermal energy). In any case, this effect was also observed in samples grown on < 100 > substrates at the same time frame as these samples, so it is not unique to the < 110 > orientation. As a result, the bandgaps were extracted from the 77K PL spectra. The 77K PL spectrum (pump power density ~ 20 W/cm^2) for the same sample of Fig. 4.4(a) is shown in Fig. 4.4(b). At 77K, thermal broadening and a band-filling effect due to the pump power (~ 20 W/cm^2) lead to broad overlapping peaks (Fig. 4.4(b-f)). The width of the peak increases as the pump power increases, indicating the band-filling effect [16].

To extract a bandgap, the 77K PL spectra were fitted using an electron-hole plasma model (EHP) [16]. The model convolves the ideal lineshape for a single electron-hole transition over all the occupied electron and hole states. Assuming constant matrix elements for both NP lines and phonon replicas for all possible transitions, all transitions in the EHP were accounted for by the following integral:

$$I(hv) = I_0 \int_0^{hv-E_{g,PL}} dE\ D_e(E) D_h(hv - E_{g,PL} - E) f(E, F_e, T) f(hv - E_{g,PL} - E, F_h, T) \tag{4.1}$$

where D_e and D_h are the densities of states of electrons and holes, respectively, hv is the photon energy, $E_{g,PL}$ is the PL bandgap, and f is the Fermi function for electrons and holes. The electron Fermi energy F_e and hole Fermi energy F_h are determined by carrier densities and linked through charge neutrality.

Note that if we have $D_e \sim (E - E_c)^\alpha$ and $D_h \sim (E_v - E)^\beta$, the line shape near the bandgap can be simplified as

$$I(hv) \sim (hv - E_{g,PL})^{(\alpha+\beta+1)} \tag{4.2}$$

In the case of quantum well samples, the densities of states are constant, i.e., $\alpha =$